The role of traction in membrane curvature generation

Haleh Alimohamadi[1+], Ritvik Vasan[1+], Julian E. Hassinger[2], Jeanne C. Stachowiak[3], Padmini Rangamani[1*]

[1]Department of Mechanical and Aerospace Engineering, University of California San Diego, La Jolla, CA 92093; [2]Biophysics Graduate Group, University of California Berkeley, Berkeley, CA 94720
[3]Department of Biomedical Engineering, University of Texas at Austin, Austin, TX 78712

Abstract

Membrane curvature can be generated by a variety of different molecular mechanisms such as protein scaffolding, heterogeneity, cytoskeletal forces that act as inputs. These mechanisms have the net effect of generating stresses on the bilayer that are translated into distinct final shapes of the membrane as outputs. We sought to reverse this input-output relationship by using the observed shape of a curved membrane to extract physical quantities such as the magnitude of the applied forces acting on the bilayer. To do this, we first calculated the normal and tangential tractions along the membrane surface using the shape and material properties of the bilayer. Then, externally applied forces were computed by taking a contour integral of tractions on the region boundary. We applied this approach to three different examples to demonstrate its utility - membrane tube formation, emergence of line tension at the interface of two spontaneous curvature fields, and the formation of podosome protrusions in human macrophage cells. These examples demonstrate that this analysis and accompanying workflow can be used to extract meaningful measurements of force and line tension from membrane shapes in a wide variety of biological contexts.

*Corresponding author: prangamani@ucsd.edu

+These authors contributed equally to this work

Keywords Membrane curvature, Lipid bilayer, Helfrich energy, Traction, Budding, Tether formation.

Introduction

Cell shape plays an important role in regulating a diverse set of biological functions including development, differentiation, motility, and signal transduction [1–4]. In addition, the ability of cellular membranes to bend and curve is critical for a variety of cellular functions including membrane trafficking processes, cytokinetic abscission, and filopodial extension [5, 6]. In order to carry out these functions, cells harness diverse mechanisms of curvature generation including compositional heterogeneity [7, 8], protein scaffolding [9], insertion of amphipathic helices into the bilayer [10], and forces exerted by the cytoskeleton [11]. Reconstituted and synthetic membrane systems also exhibit a wide range of shapes in response to different curvature-inducing mechanisms including steric pressure due to intrinsically disordered proteins [12] and protein crowding [13]. These effects can be interpreted as input-output relationships, where the input is the protein distribution, lipid or protein asymmetry or the forces exerted by the cytoskeleton and the output is the observed shape of the membrane (Fig. 1A).

It is well-known that the various curvature-inducing mechanisms induce surface stresses; expressions for these stresses have been derived using either variational methods [14–17] or by using auxiliary variables that enforce geometric constraints [18, 19]. However, only a few efforts have focused on calculating stresses from experimentally observed membrane deformations. Lee et al. suggested that membrane shape itself acts as a reporter of applied forces [20] and calculated the axial force required to form membrane tethers based on shape alone. They showed that the calculated value of force was in excellent agreement with their experimental measurements. Separately, Baumgart and colleagues showed that the Gaussian modulus has a strong effect on membrane budding in phase-separated vesicles and that its magnitude can be obtained by analyzing the geometry of the vesicle alone [7, 8]. Despite these examples, there remains a disconnect between theoretical analysis of surface stresses and experimental observations of membrane shape.

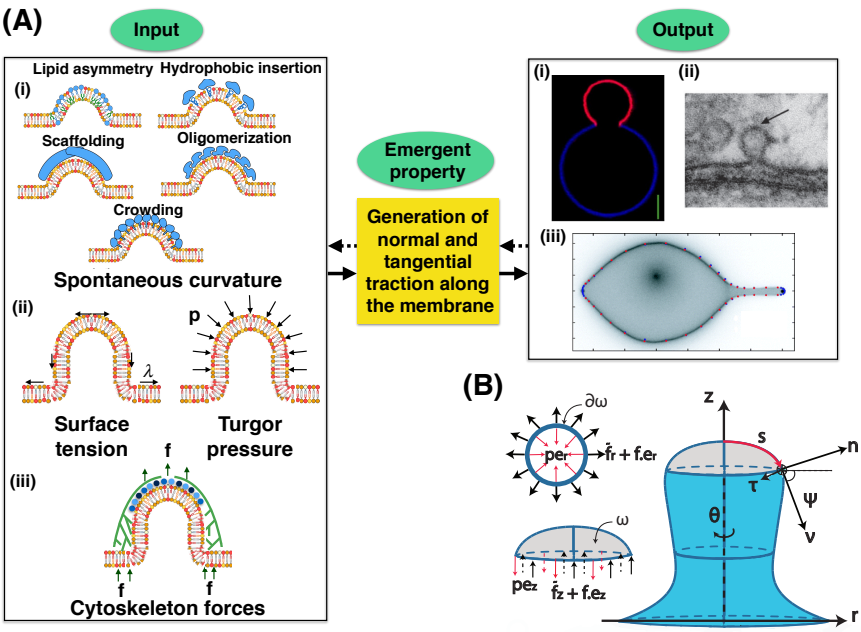

Figure 1: Membrane curvature generation as an input-output relationship. (A) Membrane curvature is controlled by different physical inputs including (i) protein-induced spontaneous curvature, (ii) membrane tension and turgor pressure, and (iii) forces exerted by the cytoskeleton. These curvature generating mechanisms exert normal and tangential tractions on the membrane resulting in different shapes – for example, (i) an axially symmetric vesicle with fluid phase coexistence visualized via two-photon fluorescence microscopy [8], (ii) a synaptic vesicle visualized by electron microscopy [21], and (iii) tether formation using optical tweezers [20]. (B) A schematic representing the axisymmetric coordinate system used for calculating curvature and traction. Inset shows that pressure opposes traction and external force in both the radial and axial directions.

We sought to bridge this disconnect by developing a general framework for the analysis of experimentally observed membrane shapes. In essence, we seek to invert the input-output relationship of Figure 1 by using the shape of the membrane as an input to calculate the tractions and force distributions along the membrane, which can give insight into various mechanisms of membrane bending. This work is timely as a number of imaging modalities are capable of generating high-resolution images of membrane deformations both *in vivo* and *in vitro*. Taking advantage of such images, we apply this framework to three distinct classes of membrane deformations – tethers, buds, and actin-rich podosome protrusions– and provide a physical interpretation for the normal and tangential traction distributions. Thus, our work extends the notion of curvature-induced surface stresses to increasingly complex biological phenomena.

Methods

Model Development

Assumptions

We assume that the curvature of the membrane is much larger than the thickness of the bilayer and that the lipid bilayer can be modeled as a thin elastic shell using the Helfrich-Canham energy model [22]. We also assume that the membrane is areally incompressible because the energetic cost of stretching the membrane is high [23]; this constraint is implemented using a Lagrange multiplier as discussed in [14]. For the present derivation, we assume that bending and Gaussian moduli are uniform throughout the membrane (a case in which this assumption is relaxed is given in the SOM). Finally, for simplicity in the numerical simulations, we assume that the membrane in the region of interest is either rotationally symmetric (Fig. 1B) or the out-of-plane membrane deformation is small and we can parameterize our system by a 1D Monge gauge [24].

Helfrich energy and equations of motion

We use a modified version of the Helfrich energy that includes spatially-varying spontaneous curvature $C\left(\theta^{\alpha}\right)$, [25–28],

Table 1: Notation used in the model

Notation	Description	Units
W	Local energy per unit area	$\mathrm{pN/nm}$
p	Pressure difference across the membrane	$\mathrm{pN/nm^2}$
C	Spontaneous curvature	$\mathrm{nm^{-1}}$
θ^α	Parameters describing the surface	
$\mathbf{n}$	Normal to the membrane surface	unit vector
$\mathbf{a}_\alpha$	Basis vectors describing the tangent plane	
λ	Membrane tension, $-(W+\gamma)$	$\mathrm{pN/nm}$
H	Mean curvature of the membrane	$\mathrm{nm^{-1}}$
K	Gaussian curvature of the membrane	$\mathrm{nm^{-2}}$
κ	Bending modulus	$\mathrm{pN \cdot nm}$
κ_G	Gaussian modulus	$\mathrm{pN \cdot nm}$
$\mathbf{f}$	Applied force per unit area	$\mathrm{pN/nm^2}$
$\tilde{f}$	Traction	$\mathrm{pN/nm}$
$\tilde{f}_n$	Component of the traction in the normal direction	$\mathrm{pN/nm}$
$\tilde{f}_\nu$	Component of the traction in the tangential direction	$\mathrm{pN/nm}$
$\tilde{F}_z$	Calculated force in axial direction	pN
ξ	Energy per unit length	pN

$$W = \kappa \left[H - C(\theta^\alpha)\right]^2 + \kappa_G K. \tag{1}$$

where W is the energy per unit area, H is the local mean curvature, and K is the local Gaussian curvature. θ^α denotes the surface coordinates and this form of the energy density accommodates the local heterogeneity in the spontaneous curvature C. Note that W differs from the standard Helfrich energy by a factor of 2, which is accounted for by using the value of κ to be twice that of the standard bending modulus typically encountered in the literature (See Table 1 for notation).

The "shape equation", which gives the first functional normal variation of this energy is given by [14, 25]

$$\underbrace{\Delta\left[\kappa\left(H-C\right)\right] + 2\kappa\left(H-C\right)\left(2H^2-K\right) - 2\kappa H\left(H-C\right)^2}_{\text{Elastic Effects}} - \underbrace{\left(p+2\lambda H\right)}_{\substack{\text{Capillary}\\ \text{effect}}} = \underbrace{\mathbf{f}\cdot\mathbf{n}}_{\substack{\text{External}\\ \text{force}}}, \tag{2}$$

where Δ is the surface Laplacian operator, p is the pressure difference across the membrane, λ is interpreted as the membrane tension [25, 28], $\mathbf{f}$ is a force per unit area — not necessarily normal to the membrane — applied to the membrane surface, and $\mathbf{n}$ is the unit normal to the surface [26]. The tangential variation, accounting for the heterogenous protein-induced spontaneous curvature, heterogeneous moduli, and externally applied force, results in a spatial variation of λ [26, 28]. This is given by

$$\underbrace{\lambda_{,\alpha}}_{\substack{\text{Gradient of}\\ \text{surface tension}}} = \underbrace{2\kappa\left(H-C\right)\frac{\partial C}{\partial \theta^\alpha}}_{\text{protein-induced variation}} - \underbrace{\mathbf{f}\cdot\mathbf{a}_\alpha}_{\substack{\text{External}\\ \text{force}}}, \tag{3}$$

where $(\cdot)_{,\alpha}$ is the partial derivative with respect to the coordinate α and $\mathbf{a}_\alpha$ is the unit tangent in the α direction. A complete derivation of the stress balance and the governing equations of motion, including the effect of variable bending and Gaussian moduli, is presented in the Supplementary online material (SOM).

Surface stress tensor and traction calculation

We define the force balance along a surface ω bounded by a parallel line of constant θ^α and the bounding curve denoted by $\partial\omega$ as

$$\underbrace{\int_{\omega} p\mathbf{n}da}_{\substack{\text{Force due to pressure}\\ \text{acting on the surface}}} + \underbrace{\int_{\partial\omega} \tilde{\mathbf{f}}dt}_{\substack{\text{Traction force}\\ \text{along the boundary}}} = 0, \tag{4}$$

where $\tilde{\mathbf{f}}$ represents the traction along a curve bounded by t. Traction, which is the force per unit length, was initially introduced by physicists as a result of Noether's theorem [15, 16, 18]. This theorem states that for any elastic surface that is in equilibrium, there exists a unique traction distribution such that its divergence is conserved [18]. Mechanically, the traction distribution gives us information about the response of the membrane to externally applied loading including forces acting on the membrane or protein-mediated bending.

While Eq. 4 is a general expression independent of coordinates, we will restrict further analysis to two cases for ease of analysis – a) axisymmetric coordinates (Fig. 1B) and b) 1D Monge gauge [24].

Case I: Axisymmetric coordinates

The axisymmetric coordinate system is defined by the position vector along the surface as follows

$$\mathbf{r}(s,\theta) = r(s)\mathbf{e}_r(\theta) + z(s)\mathbf{k}. \tag{5}$$

Here $(\mathbf{e}_r, \mathbf{e}_\theta, \mathbf{k})$ form an orthogonal coordinate basis and $r(s)$ and $z(s)$ are the radius and elevation from the axis of revolution and base plane respectively (see SOM for full derivation of surface parameters). The complete parametrization is given in the SOM. Since $(r')^2 + (z')^2 = 1$, where $(')$ denotes derivative with respect to the arc length, we define an angle ψ made by the tangent along the arc length with the horizontal such that $r'(s) = \cos\psi$ and $z'(s) = \sin\psi$. The traction acting on a curve of constant z is given by

$$\tilde{\mathbf{f}} = \tilde{f}_\nu \boldsymbol{\nu} + \tilde{f}_n \mathbf{n}. \tag{6}$$

where $\tilde{f}_n$ and $\tilde{f}_\nu$ are defined in [17] and including the spontaneous mean curvature, we obtain

$$\tilde{f}_n|_{\text{axisy}} = -\kappa(H' - C'), \tag{7a}$$
$$\tilde{f}_\nu|_{\text{axisy}} = \kappa(H - C)(H - C - \psi') + \lambda. \tag{7b}$$

Case II: Monge parametrization

The position vector in the Monge gauge is given as

$$\mathbf{r}(x) = x\mathbf{e}_1 + z(x)\mathbf{e}_3, \tag{8}$$

where $(\mathbf{e}_1, \mathbf{e}_3)$ are the unit vectors in 'x' and 'z' direction. For small deformations ($z_{,x} \ll 1$), $2H = z_{,xx}$, and $K \approx 0$ everywhere on the membrane. The normal and tangential tractions are given by [19]

$$\tilde{f}_n|_{\text{Monge}} = -\kappa(H' - C'), \tag{9a}$$
$$\tilde{f}_\nu|_{\text{Monge}} = \kappa(H - C)(H - C - H_{,xx}) + \lambda. \tag{9b}$$

Interpretation of traction

Numerous studies have derived these equations mathematically and explained them in a biophysical context. Capovilla and Guven [15–17] explained this based on the action-reaction law – if one were to cut the membrane along any curve, $\tilde{f}_n$ and $\tilde{f}_\nu$ are the forces per unit length of the curve in the normal and tangential directions respectively, that the membrane on one side of the cut exerts on the other. Deserno [29] used an electrostatics analogy for clarifying the logic of force calculation from the flux of traction through a closed boundary. The expressions for tractions (Eqs 7a, 7b) reduce to their corresponding fluid analogues for negligible membrane rigidity and pressure difference. Thus, we can interpret the normal and tangential traction as follows – the tangential traction distribution tracks the gradient in 'effective' surface tension while the normal traction distribution contains information regarding a force balance performed normal to the membrane at every point. Further physical interpretations of these quantities, which have units of force per unit length or energy per unit area, can be obtained based on the particular biological phenomena.

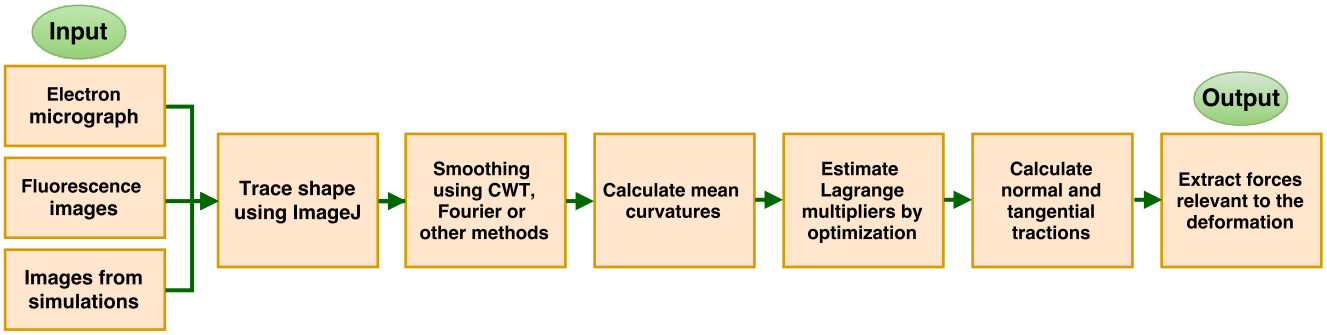

Figure 2: Flowchart outlining the algorithm for using shape as input and extracting force as output. The input to this framework can be images from experimental methods (fluorescence and electron microscopy) or from simulations. The details of the methods and fitting algorithms are outlined in the SOM. Briefly, we trace the shape of the membrane from the image and use smoothing techniques such as coupled wavelet transform (CWT) or Fourier transforms to reduce noise and increase the accuracy of obtaining derivatives (see Fig. S1). Then, we use these traced contours to calculate the curvatures, estimate Lagrange multipliers, and calculate surface stresses to obtain forces relevant to the deformation. Finally, the applied forces are calculated by traction integral around a closed boundary of interest.

Development of an image analysis framework

In order to understand how the normal and tangential tractions can be interpreted in different experimental contexts, we developed a framework that takes images from either experiments (both fluorescence images and electron micrographs) or from simulations and used a shape tracing and fitting algorithm to obtain the mean and Gaussian curvature along the curve (Figure 2). We then estimate the Lagrange multipliers using an optimization algorithm, and using these, we calculate the surface stresses and the forces relevant to that particular deformation. Thus, we implement the inverse problem of using membrane shape as an input and extract forces as the output. Details of each step in our framework are provided in the SOM.

Results

Tether formation due to applied load – revisiting a classical membrane deformation

The formation of membrane tethers in response to a point load is a classic example of force-mediated membrane deformation [30, 31] that has been studied both experimentally [32, 33] and theoretically [34, 35] by many groups. We used this example to validate our method and to identify how normal and tangential tractions contribute to the formation of tethers. We first conducted simulations using a localized force at the pole to mimic a point load and solved Eqs. S25 using the 'bvp4c' solver in MATLAB (details provided in SOM) for a membrane tension of 0.02 $\mathrm{pN/nm}$. We used the resulting equilibrium shapes as input to the framework shown in Fig. 2.

The normal and tangential traction distributions along the tether are showed in Figs. 3A, B. The absolute value of the normal tractions are highest at the pole as the applied force increases. The membrane curves away from the applied force along the region over which it is applied and conforms to a stable cylindrical geometry along the rest of the tether and a flat region at the base. The tangential traction has a large positive value along the cylindrical portion of the tether (Fig. 3B) showing that the membrane resists stretching as the tube is pulled out. The tether cap has negative tangential traction because of the membrane tension heterogeneity (Eq. S21).

From the traction distribution, we can calculate the applied axial force on the membrane by integrating the axial component of the total force (see SOM) along the circumference of the bounding curve $\partial\omega$ to obtain

$$\tilde{F}_z = 2\pi r \Big[\underbrace{\kappa H' \cos\psi + \kappa H (H - \psi') \sin\psi}_{\text{Bending contribution}} + \underbrace{\lambda \sin\psi}_{\substack{\text{Tension}\\ \text{contribution}}} \Big], \tag{10}$$

where $\tilde{F}_z$ is the axial force generated in response to the external load. We show that the negative of Eq. 10, evaluated at the base of the geometry, exactly matches the force-extension relationship for tether formation (Fig. 3D), validating our method. This force match can be recreated for simulations with pressure by modifying our expression for force (Eq.S40, see Fig. S3 and Fig. S4). Likewise, the axial traction at every mesh point can be matched to a combination of traction due to pressure and

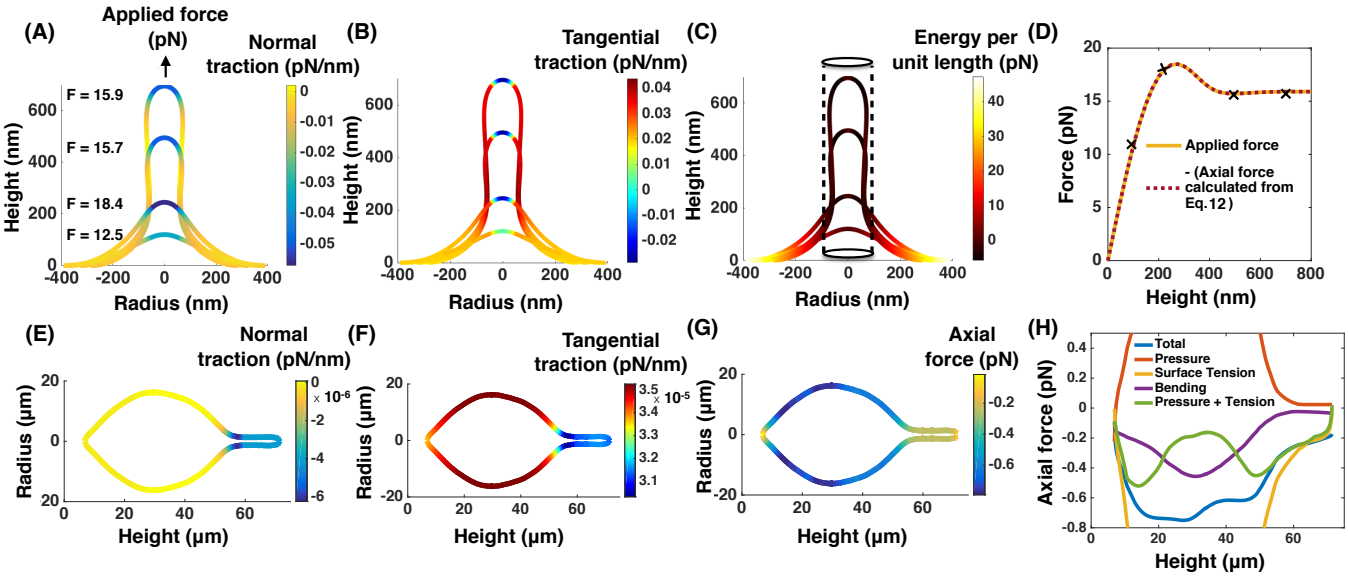

Figure 3: Analysis of normal and tangential traction for membrane tethers. (A) Normal traction distribution along four membrane tether shapes obtained by applying a point load of the specified magnitude at the pole, $\lambda = 0.02\,\mathrm{pN/nm}$, $\kappa = 320\,\mathrm{pN \cdot nm}$. (B) Tangential traction distribution along the membrane shapes for conditions shown in (A). (C) Energy per unit length calculated using Eq. 11 along the four membrane shapes shown in (A). The dashed lines outline the equilibrium geometry for a membrane cylinder, $\mathrm{R_{cylinder}} = \frac{1}{2}\sqrt{\frac{\kappa}{\lambda}}$. (D) Magnitude of axial force as a function of tether height, showing an exact match between the force (Eq. 10) calculated from the traction distribution and obtained directly from the simulation. (E) Normal traction distribution along a fluorescence image of a vesicle in a tether pulling experiment from [20], $\kappa = 2 \times 0.85 \times 10^{-19}$ J, where κ is twice that of the standard bending modulus. The traction distribution along tether resembles the distribution seen in (A) while the normal traction along the vesicle is zero because of the near spherical geometry. (F) Tangential traction distribution along the vesicle. (G) Axial force along the vesicle, ~ 0.7 pN along most of the vesicle and a smaller axial force of ~ 0.3 pN at the tether. (H) Axial force and its components as a function of axial distance along the vesicle.

external force (Eq. S40), shown in Fig. S5 for a tether pulling simulation against a large pressure of 1 MPa observed in yeast endocytosis [36].

We also found that radial stresses play an important role in squeezing the membrane neck and holding the cylindrical configuration during membrane elongation (see Fig. S2). The energy per unit length, ξ, associated with this circular deformation can be found by integrating the radial traction along the curve $\partial\omega$ (Fig. 1B), as

$$\xi = 2\pi r\Big[\underbrace{\kappa H(H-\psi')\cos\psi}_{\substack{\text{Curvature}\\\text{contribution}}} + \underbrace{\lambda\cos\psi}_{\substack{\text{Tension}\\\text{contribution}}} + \underbrace{\kappa H'\sin\psi}_{\substack{\text{Curvature}\\\text{gradient}\\\text{contribution}}}\Big]. \tag{11}$$

ξ can be interpreted as an 'effective' line tension [37], shown in Fig. 3C. While line tension denotes the force acting at the boundary of two interfaces – e.g. inward force for a liquid droplet on a hydrophobic substrate and an outward force on a hydrophilic substrate [38], the 'effective' line tension predicts a general resistive force acting at every point opposing any change in the membrane length, regardless of a phase boundary. Consequently, the point of zero 'effective' line tension tell us the nature of the equilibrium geometry, shown as the dotted cylinder. The radius of the cylinder can also be evaluated by minimizing the free energy, giving $\mathrm{R_0} = \frac{1}{2}\sqrt{\frac{\kappa}{\lambda}}$ [34]. This equilibrium cylinder has no curvature gradient, leading to zero 'effective' line tension. The calculated values of energy per unit length inside the cylinder are negative while those outside are positive, indicating that the 'effective' line tension determines the extent of deviation from the equilibrium geometry. Additionally, the value of ξ at the neck is ~ 3pN, providing an estimate of the effective line tension required to form a neck in tethers.

Having validated the model, we sought to apply our method to experimental observations of tethers. We used previously published images of vesicles with tethers [20] to calculate the traction distributions along the tether using the procedure described in Fig. 2. Lagrange multipliers were estimated using an equilibrium force density minimization procedure (see SOM

for details) and calculated as p = $6.3 \times 10^{-9}\,\mathrm{pN/nm^2}$, λ = $4.36 \times 10^{-5}\,\mathrm{pN/nm}$ and C = $-1 \times 10^{-4}\,\mathrm{nm^{-1}}$, which closely matches the parameters given in [20]. We would like to note that the spontaneous curvature calculated using our optimization algorithm is a shift in mean curvature (Eq. S17), while the reported spontaneous curvature in [20] is a rescaling of principle curvature summation. We also used twice the reported value of bending modulus $\kappa = 0.85\ \times 10^{-19}$ J [20]. Our analysis of the experimental images shows that the distribution of normal traction along the tether resembles that of Fig. 3A – normal traction is negative along the tether cap with a maximum at the neck at the region of increasing curvature gradient, while the tangential traction is positive along the tether and resists membrane stretch (Figs. 3E, F). Since the tether is connected to a spherical vesicle, we see that the normal traction becomes negligible and tangential traction assumes a constant value along the spherical region, indicating an equilibrium geometry. We calculated the axial force accounting for the pressure difference and found that the curved portion had an average force of $0.7\,\mathrm{pN}$, and the force along the tether was $0.3\mathrm{pN}$ (Fig. 3G). This is in agreement with the reported value of the applied force as $\sim 0.6\mathrm{pN}$ along the entire membrane [20]. Furthermore, the different contributions of pressure, tension, and bending follow the same profile as that reported in [20] (Fig. 3H), indicating that we can not only extract the applied forces on the membrane using shape information but also evaluate contributing terms.

Formation of buds due to spontaneous curvature is characterized by emergent line tension

Phase separation and lipid domains are classical mechanisms of bud formation and vesiculation [39]. Previously, we and others have shown that protein-induced heterogeneity on the membrane can be modeled using a spontaneous curvature field [25, 28, 40]. We used this framework to investigate the nature of membrane tractions generated during budding due to a spontaneous curvature field. We conducted simulations for a constant area of the spontaneous curvature field $\mathrm{A} = 10,000\,\mathrm{nm}^2$ and varied the extent of spontaneous curvature from $C = 0\ \mathrm{nm}^{-1}$ to $C = -0.032\ \mathrm{nm}^{-1}$. We chose three distinct shapes – a shallow bump, a U-shaped bud, and a closed Ω- shaped bud as inputs and calculated the normal and tangential tractions (Fig. 4A, B). We observed that the normal traction is negative along the applied spontaneous curvature field indicating a sharper change in mean curvature compared to the applied asymmetry ($H' > C'$ in Eq. 7a). At the neck, where $\psi = \frac{\pi}{2}$, normal traction is maximum and acts purely inward, representing the tendency of the membrane to form small necks. The tangential traction shows a change in sign from positive to negative as the neck radius becomes smaller. This change in sign highlights the critical role of the gradient in tangential traction in the formation of narrow necks [26] (Fig. 4B). The positive tangential traction in tent-like small deformations indicates that the membrane resists the bending deformation; however, in the U-shaped and closed buds, the negative tangential traction along the cap acts to pull the membrane inward and favors the adoption of a highly curved shape. Additionally, projecting the local traction onto the radial and axial directions reveals that bud formation by spontaneous curvature is purely driven by evolution of radial traction while axial traction is zero everywhere Fig. S6.

The energy per unit length was evaluated along the membrane using a modified version of Eq. 11 to include the spontaneous curvature (Eg. S42a) (Fig. 4C). The dashed circles represent the equilibrium spherical vesicles calculated by Helfrich energy minimization ($R_{\text{vesicle}} = \frac{\kappa C}{\lambda + \kappa C^2}$) [26]. Each equilibrium vesicle divides the space into two domains – (*i*) the membrane inside the vesicle with negative energy per unit length that bends to form a bud (*ii*) the membrane outside the vesicle with positive energy per unit length that resists such a deformation. Previously, both modeling and experimental studies have shown that in heterogeneous membranes line tension can be sufficient for scission of endocytic pits [41] or the formation of buds in vesicle experiments [7, 8]. In the case of applied spontaneous curvature field, the modified expression of energy per unit length (Eq. S42a) can be interpreted as an actual line tension at the interface of the two phases. Through the process of bud formation, line tension undergoes a sign change from positive (acting outward) to negative (acting inward), effectively transitioning from a tension-dominated regime to a curvature gradient-dominated regime (Fig. 4D). This transition from positive to negative line tension with increasing value of spontaneous curvature is also observed in other studies [42]. The value of the energy per unit length at the interface varies between -5 pN to 5 pN, which is of the order of the reported interfacial line tension between coexisting phases in lipid bilayers [41, 43]. We also see that once the overhang develops, closing the neck requires a smaller line tension and this value varies based on the type of reservoirs affecting the line tension at the interface (see Figs. S7, S8).

We traced images of budding in phase-separated giant unilamellar vesicles (GUVs) from [8] and calculated normal and tangential tractions along the vesicle shape to see if our estimates of line tension were meaningful. The constant parameters in Eqs. (S43a, S43b) are chosen based on reported values in this paper, while the spontaneous curvature for each vesicle is estimated by the equilibrium force density minimization method. A rendering of the original image is shown in Fig. 5A. The normal traction distribution along the membrane is almost zero everywhere except at the neck, which is the interface of the lipid disordered and ordered phase (Fig. 5B). The corresponding energy per unit length at the neck (Eq. S46a) has a value of $0.65\,\mathrm{pN}$, comparable to the experimentally obtained value of $0.67\,\mathrm{pN}$ [8], indicating that using a few material parameters and the shape, we are able to extract the value of line tension at the interface. We note here that the value of line tension obtained

is sensitive to the gradient in spontaneous curvature C, which is applied as a hyperbolic tangent function Eq. S30 and so we chose the width and slope of the transition region to ensure a smooth function across the region of heterogeneity. Fig. S9 shows similar behavior for two other experimental vesicle shapes [8].

We next asked if we could extract meaningful values of tractions from cell-based experiments. We used electron micrographs that depict the synaptic membrane undergoing clathrin-mediated endocytosis in chromaffin cells from [21] (Fig. 6A). Since these images are not symmetric, we converted them to conform to axisymmetric coordinates using cubic interpolation schemes (Fig. 6B). Here, the coat was projected onto the plasma membrane such that the tangent angle at both points were equal. Parameters such as spontaneous curvature and surface tension are estimated to be C = -0.01 nm^{-1} and λ = 0.016 $\mathrm{pN/nm}$ respectively using force density minimization. We used parameters to match documented values for neuronal membranes, including a bending modulus of κ = 320 $\mathrm{pN/nm}$ [44]. From the normal traction distribution along the Ω profile (Fig. 6C), we see that the normal traction is large and negative at the edge of the protein coat. This results in value of line tension of approximately 12 pN using a spontaneous curvature transition transition similar to that used in Figs. 4, 5. This calculated value of line tension is in agreement with other reported values of line tension [41, 43]. The tangential traction distribution (Fig. 6D) is similar to that observed in Figs. 4 B, 5 C, indicating that despite the molecular complexity present in cells, using our framework, we can obtain insight into the forces underlying membrane curvature generation.

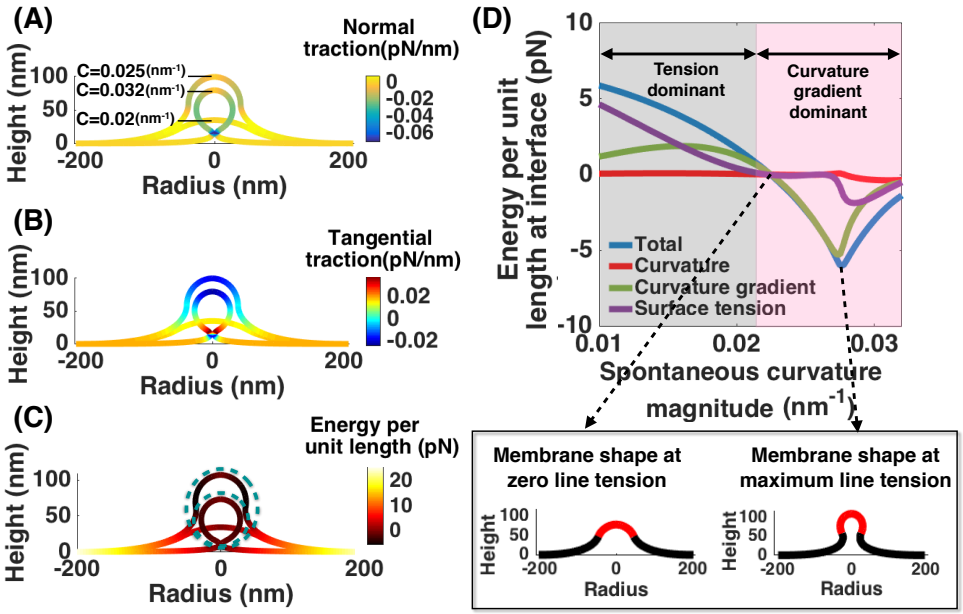

Figure 4: Analysis of budding due to protein-induced spontaneous curvature and calculation of line tension. Simulations were conducted with (A =10,053 nm^2) spontaneous curvature at the center of an initially flat patch increasing from $C = 0$ to $C = 0.032\,\mathrm{nm}^{-1}$, $\lambda = 0.02\,\mathrm{pN/nm}$, $\kappa = 320\,\mathrm{pN}\cdot\mathrm{nm}$, $p = 0\,\mathrm{pN/nm}^2$ [26]. (A) Normal traction along the membrane for three different spontaneous curvature distributions. (B) Tangential traction distribution along the shapes shown in (A); (C) Energy per unit length distribution for the three different shapes. The dashed line circles outline spheres with mean curvatures $H = 0.032\,\mathrm{nm}^{-1}$ (smaller circle) and $H = 0.025\,\mathrm{nm}^{-1}$ (larger circle). (D) Change in energy per unit length and its components at the interface with increasing spontaneous curvature. Two regimes are observed: a surface tension-dominated regime for small values of spontaneous curvature and a curvature gradient-dominated regime for large vales of spontaneous curvature. The membrane configurations are shown for two spontaneous curvature $C = -0.02\,\mathrm{nm}^{-1}$, where energy per unit length at interface is zero and $C = -0.025\,\mathrm{nm}^{-1}$, where energy per unit length is maximum. The red domains show the region of spontaneous curvature for the corresponding shapes.

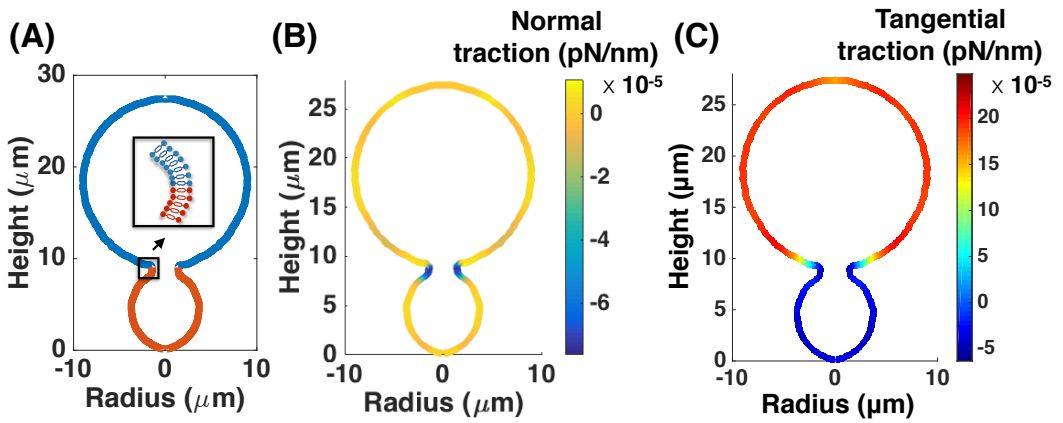

Figure 5: Calculation of line tension at the interface of two lipid domains. Normal and tangential tractions were calculated along published [8] two-photon microscopy images of axially symmetric vesicles with fluid phase coexistence. The constants used were $p = 2.8 \times 10^{-2}\,\mathrm{N/m^2}$, surface tension of disordered phase $\lambda_d = -1.03 \times 10^{-4}\,\mathrm{mN/m}$, surface tension of ordered phase $\lambda_o = -0.91 \times 10^{-4}\,\mathrm{mN/m}$, bending modulus of disordered phase $\kappa_d = 10^{-19}$ J, ratio of bending moduli $\kappa_o/\kappa_d = 5$ and absolute difference in gaussian moduli $\Delta\kappa_G = 3.6 \times 10^{-19}$ J [8]. Spontaneous curvature was estimated by the equilibrium force minimization, $C_o = -0.63\,\mu\mathrm{m}^{-1}$ and $C_d = -0.75\,\mu\mathrm{m}^{-1}$. (A) Contour of a vesicle with lipid ordered phase L_o (Blue) and lipid disordered phase L_d (Red) traced using ImageJ. (B) Normal traction distribution along the vesicle, showin a large negative normal traction at the interface. The energy per unit length at this point (where$\psi = \frac{\pi}{2}$ and $\tilde{f}_n = \tilde{f}_r$) is $0.65\,\mathrm{pN}$, similar to the value of line tension, $0.67\,\mathrm{pN}$, obtained by Baumgart and colleagues [8]. (C) Tangential traction distribution along the vesicle. The tangential traction is negative everywhere and L_d phase has a larger magnitude of tangential traction while L_o phase has a smaller value, leading to a gradient at the interface.

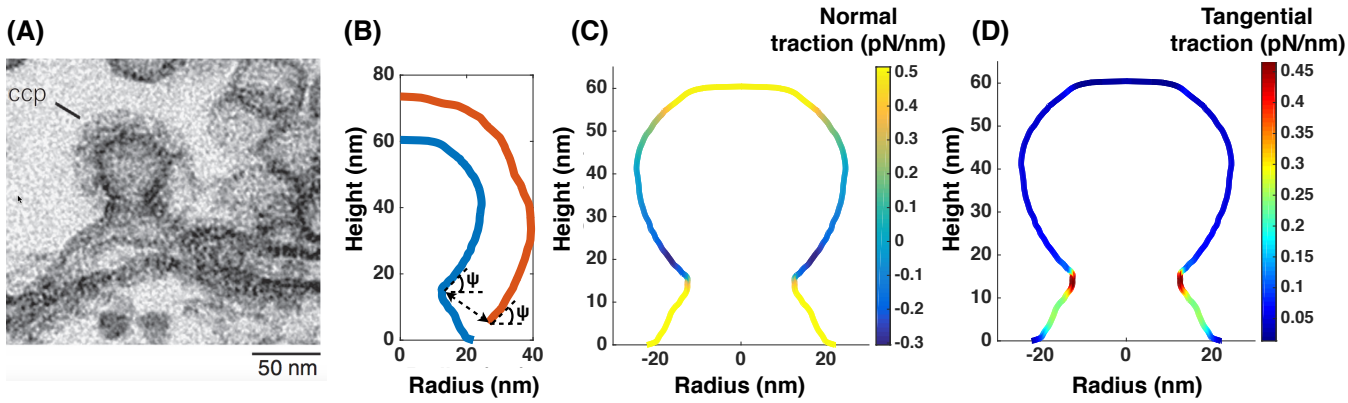

Figure 6: Analysis of traction distribution of endocytic buds in chromaffin cells. (A) Electron micrograph of an Ω-shaped profile of a clathrin-coated pit in a reticulospinal synapse of a chromaffin cell [21]. (B) Axisymmetric projection of membrane and protein coat. Tracing of the membrane and protein coat are done using ImageJ. The edge of the protein coat is projected onto the point on the membrane with same tangent angle ψ. (C) Normal traction distribution along the membrane, $C = -0.01\,\mathrm{nm}^{-1}$, $\lambda = 0.016\,\mathrm{pN/nm}$, $\kappa = 320\,\mathrm{pN/nm}$. (D) Tangential traction distribution shows a gradient at the interface, similar to Figs. 4 B, 5 C.

Analysis of podosome profiles of human macrophage cells yields stress tensor distribution

Podosomes or invadosomes are actin-rich protrusions of cells that are oriented perpendicular to the substrate and have a circumferential ring of adhesion proteins located at the base [47]. They are typically found in monocytic cells, endothelial cells and smooth muscle cells [47]. Multiple groups have worked on calculating the protrusive forces generated by podosomes on the substrate using atomic force microscopy (AFM) and developing different theoretical models to identify the mechanisms

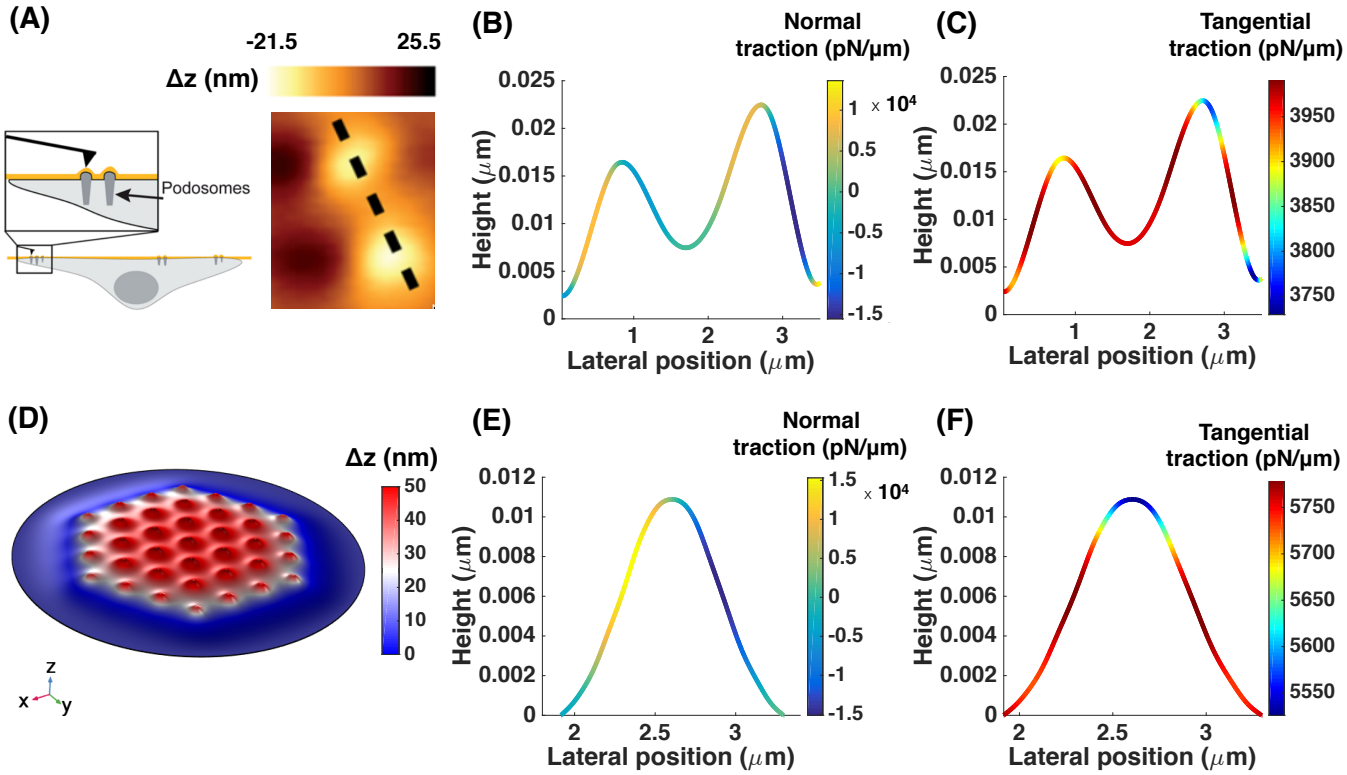

Figure 7: Actin-mediated forces in podosomes can be calculated from 1D cut sections. We analyse podosome protrusion profiles from simulations and experiments [45] using our analysis pipeline (Fig 2). We use a Young's modulus of E = 2.3 GPa [46]. (A) Schematic of human macrophage podosome-induced protrusion in a thin formvar membrane (Left) [45] with a force microscopy (PFM) image of the membrane topology (Right). (B) Normal traction distribution along the profile of the black dotted line in (A). The distribution is governed by curvature gradients. Calculating axial force (Eq. S53) at the base gives a value of 31 nN, consistent with AFM measurements done in experiments [45]. (C) Tangential traction distribution along the profile. The distribution is governed by curvature. (D) A COMSOL simulation showing protrusion profiles of a hexagonal lattice of 37 podosomes onto a formvar membrane. Protrusive force at the core of each podosome is 10 nN. (E) Normal traction distribution for a single podosome along the black line in (D). Distribution is similar to (B) and is governed by curvature gradients. Axial force at the base (Eq. S53) gives a value of 9 nN, which is close to the value of 10 nN used in the simulation. (F) Tangential traction distribution along the cut section profile.

underlying force generation [46, 48]. Detailed maps of stresses and forces on the substrate deformed by podosomes were recently reported [45, 49].

We first analyzed the AFM image of the podosome (Fig 7 A); this image shows the podosome protrusion of human primary monocyte-driven macrophages onto a formvar membrane [45]. Using the Monge gauge parametrization (Eqs. 9a, 9b), we calculated the normal and tangential traction distributions along the black dotted line in Fig. 7A. We estimated bending modulus using $\kappa \sim \mathrm{E}\mathrm{h}_f^3$, where E is young's modulus and h_f is the thickness of the formvar membrane [46, 50] and membrane tension was calculated using an optimization procedure. Given that the height of the podosome is small compared to the lateral position, the axial traction is dominated by the normal traction (S52). Calculating an accurate force value for the podosome requires many more cut sections to fill out a 2D surface. However, by assuming that the axial traction values at the base of the podosome are constant along the circumference, we calculated an approximate value for the protrusion force (Eq. S53) exerted by the podosome onto the substrate. We found this value to be equal to 31 nN over the two podosome protrusion profiles, which is consistent with experimental measurements [45].

We also performed a numerical simulation of podosome protrusion, as described previously in [45, 46]. We apply a local protrusion force to a surface of radius 8 $\mu\mathrm{m}$ and thickness 30 nm with clamped boundary condition. Protrusion force was modelled as an upward force of 10 nN at the podosome core and a downward force of 10 nN adjacent to the core to result in the podosome profile shown in Fig 7 D. Additional details provided in the SOM. We took the protrusion profile of a single

podosome along the black line shown in (D) and passed it through the framework in Fig. 2 using a linear Monge gauge to determine traction distributions (Eqs. 9a, 9b). Membrane tension was calculated using the optimization procedure.

Analysis of the normal traction distribution (Fig 7E) shows that the normal traction changes sign on either side of the shape, similar to Fig. 7B, which is a consequence of the curvature gradient [17, 19]. The tangential traction distribution due to membrane tension is shown in Fig 7F. We observe that the the profile of the tangential traction is constant along the shape, with a smaller value along the cap, which is a consequence of the curvature. We then calculated the average axial traction at the base and used Eq. S53 to compute an approximate value of force exerted by the podosome onto the substrate to be 9 nN, which is close to the 10 nN used in simulation.

Discussion

In this study, we presented a framework for the calculation of normal and tangential tractions for membrane deformation and demonstrated its application using three different examples of membrane deformation. In all cases, we were able to use images from different experimental modalities or simulations to calculate the traction distribution along the membrane. From these calculations, we summarize that (a) tether formation requires both normal and tangential tractions (ig. 3), (b) line tension can be calculated between two phases as an energy per unit length (Figs. 4, 5, 6), and (c) we were able to use a highly simplified framework to extract the values of net axial force associated with a podosome protrusion using the membrane shape alone (Fig. 7). Importantly, using different examples, we have demonstrated that the normal and tangential tractions on the membrane are a consequence of different mechanisms of curvature generation. Moving forward, this procedure can be useful for the analysis of forces acting on membranes, both in reconstituted systems or in cells. Further, the critical development will be needed to include details of the molecular machinery (actin orientation, actin binding proteins etc.).

In particular, we expect that analysis of the force distributions along membrane shapes will provide insight into how various input mechanisms are transduced into forces on the membrane that shape membrane curvature (Fig. 1).

Electron microscopy data has advanced considerably in resolution, enabling the visualization of membranes shapes in cells in unprecedented detail [51, 52]. This represents a new opportunity to dissect the physical mechanisms that come together to create the diversity of membrane shapes observed in cells. Additionally, the sensitivity condition in our model requires only that sufficient number of points be chosen along a shape to ensure best fits. Beyond this, we expect that the approach will be powerful for understanding how cells regulate their function through geometry, mechanics, and signaling [2].

At present it remains very difficult to dissect the combination of molecular mechanisms that are responsible for the shape of curved cellular membrane structures such as membrane buds, sheets, tubules, and filopodia [53]. For example, during the formation of coated vesicles, which are among the best studied curved cellular structures, diverse mechanisms including protein scaffolding, hydrophobic insertion, and protein crowding have each been implicated [54]. In contrast to the analysis of cellular structures, *in vitro* studies on purified proteins and lipids allow us to examine the impact of individual proteins and mechanisms on membrane shape. These data, which are abundant in the literature [13, 55, 56], can be analyzed using our method and be used to populate a database/machine-learning framework that can be then extended to analyze the shapes of complex structures in cells, which likely include contributions from multiple mechanisms. Future efforts will require the development of a broader framework to go beyond axisymmetry and small deformation regimes in continuum, and the stitching together of multiscale simulations to go from molecular models to continuum models [57, 58].

Ultimately, calculating the normal and tangential tractions on the membrane and their projection in the axial and radial directions will provide a framework for the understanding and rational design of novel mechanisms for membrane bending. For example, it has been demonstrated that PEGylation of lipids [59], amphiphilic block copolymers [60], and protein crowding [13] can curve and even induce scission of artificial lipid bilayers. Additional terms may be necessary in our formulation to account for these novel modes of membrane bending, but fundamentally there is no change to the principle of force balance that allows us to use the membrane shape as a readout of the forces. Thus, studying this inverse problem can lead to an understanding of the integration of curvature-generating mechanisms into applied forces on the membrane. This approach will allow us connect synthetic chemistry to mechanochemistry in order to engineer tools that can manipulate membrane curvature.

Acknowledgment This work was supported by ARO W911NF-16-1-0411, AFOSR FA9550-15-1-0124, and NSF PHY-1505017 grants to P.R. J.C.S. was supported by NIH R01GM112065. R.V. was supported by the UCSD Frontiers of Innovation Scholars Program (FISP) G3020. H.A. was supported by a fellowship from the Virtual Molecular Cell Consortium (VMCC), a program between UCSD and the Scripps Research Institute. J.E.H. was supported by the Department of Defense (DoD) through the National Defense Science & Engineering Graduate Fellowship (NDSEG) Program. The authors would also like to thank Prof. George Oster and Prof. David Steigmann for initial discussions, Dr. Matthew. S Akamatsu for his suggestions on improving the manuscript and Miriam Bell for critical reading..

References

1. Neves, S. R., P. Tsokas, A. Sarkar, E. A. Grace, P. Rangamani, S. M. Taubenfeld, C. M. Alberini, J. C. Schaff, R. D. Blitzer, I. I. Moraru, et al., 2008. Cell shape and negative links in regulatory motifs together control spatial information flow in signaling networks. Cell 133:666–680.

2. Rangamani, P., A. Lipshtat, E. U. Azeloglu, R. C. Calizo, M. Hu, S. Ghassemi, J. Hone, S. Scarlata, S. R. Neves, and R. Iyengar, 2013. Decoding information in cell shape. Cell 154:1356–1369.

3. Rangamani, P., M.-A. Fardin, Y. Xiong, A. Lipshtat, O. Rossier, M. P. Sheetz, and R. Iyengar, 2011. Signaling network triggers and membrane physical properties control the actin cytoskeleton-driven isotropic phase of cell spreading. Biophysical journal 100:845–857.

4. Xiong, Y., P. Rangamani, M.-A. Fardin, A. Lipshtat, B. Dubin-Thaler, O. Rossier, M. P. Sheetz, and R. Iyengar, 2010. Mechanisms controlling cell size and shape during isotropic cell spreading. Biophysical journal 98:2136–2146.

5. Mukherjee, S., and F. R. Maxfield, 2000. Role of membrane organization and membrane domains in endocytic lipid trafficking. Traffic 1:203–211.

6. Mattila, P. K., and P. Lappalainen, 2008. Filopodia: molecular architecture and cellular functions. Nature reviews Molecular cell biology 9:446–454.

7. Baumgart, T., S. T. Hess, and W. W. Webb, 2003. Imaging coexisting fluid domains in biomembrane models coupling curvature and line tension. Nature 425:821–824.

8. Baumgart, T., S. Das, W. Webb, and J. Jenkins, 2005. Membrane elasticity in giant vesicles with fluid phase coexistence. Biophysical journal 89:1067–1080.

9. Karotki, L., J. T. Huiskonen, C. J. Stefan, N. E. Ziółkowska, R. Roth, M. A. Surma, N. J. Krogan, S. D. Emr, J. Heuser, K. Grünewald, et al., 2011. Eisosome proteins assemble into a membrane scaffold. J Cell Biol 195:889–902.

10. Lee, M. C., L. Orci, S. Hamamoto, E. Futai, M. Ravazzola, and R. Schekman, 2005. Sar1p N-terminal helix initiates membrane curvature and completes the fission of a COPII vesicle. Cell 122:605–617.

11. Giardini, P. A., D. A. Fletcher, and J. A. Theriot, 2003. Compression forces generated by actin comet tails on lipid vesicles. Proceedings of the National Academy of Sciences 100:6493–6498.

12. Busch, D. J., J. R. Houser, C. C. Hayden, M. B. Sherman, E. M. Lafer, and J. C. Stachowiak, 2015. Intrinsically disordered proteins drive membrane curvature. Nature communications 6.

13. Snead, W. T., C. C. Hayden, A. K. Gadok, C. Zhao, E. M. Lafer, P. Rangamani, and J. C. Stachowiak, 2017. Membrane fission by protein crowding. Proceedings of the National Academy of Sciences 114:E3258–E3267.

14. Jenkins, J., 1977. Static equilibrium configurations of a model red blood cell. Journal of mathematical biology 4:149–169.

15. Capovilla, R., and J. Guven, 2004. Stress and geometry of lipid vesicles. Journal of Physics: Condensed Matter 16:S2187.

16. Capovilla, R., and J. Guven, 2002. Geometry of lipid vesicle adhesion. Physical Review E 66:041604.

17. Capovilla, R., and J. Guven, 2002. Stresses in lipid membranes. Journal of Physics A: Mathematical and General 35:6233.

18. Guven, J., 2004. Membrane geometry with auxiliary variables and quadratic constraints. Journal of Physics A: Mathematical and General 37:L313.

19. Fournier, J.-B., 2007. On the stress and torque tensors in fluid membranes. Soft Matter 3:883–888.

20. Lee, H. J., E. L. Peterson, R. Phillips, W. S. Klug, and P. A. Wiggins, 2008. Membrane shape as a reporter for applied forces. Proceedings of the National Academy of Sciences 105:19253–19257.

21. Wen, P. J., S. Grenklo, G. Arpino, X. Tan, H.-S. Liao, J. Heureaux, S.-Y. Peng, H.-C. Chiang, E. Hamid, W.-D. Zhao, et al., 2016. Actin dynamics provides membrane tension to merge fusing vesicles into the plasma membrane. Nature communications 7:12604.

22. Helfrich, W., 1973. Elastic properties of lipid bilayers: theory and possible experiments. Zeitschrift für Naturforschung C 28:693–703.

23. Rawicz, W., K. Olbrich, T. McIntosh, D. Needham, and E. Evans, 2000. Effect of chain length and unsaturation on elasticity of lipid bilayers. Biophysical journal 79:328–339.

24. Deserno, M., 2004. Notes on differential geometry.

25. Steigmann, D., 1999. Fluid films with curvature elasticity. Archive for Rational Mechanics and Analysis 150:127–152.

26. Hassinger, J. E., G. Oster, D. G. Drubin, and P. Rangamani, 2017. Design principles for robust vesiculation in clathrin-mediated endocytosis. Proceedings of the National Academy of Sciences 114:E1118–E1127.

27. Agrawal, A., and D. J. Steigmann, 2009. Boundary-value problems in the theory of lipid membranes. Continuum Mechanics and Thermodynamics 21:57–82.

28. Rangamani, P., K. K. Mandadap, and G. Oster, 2014. Protein-induced membrane curvature alters local membrane tension. Biophysical journal 107:751–762.

29. Deserno, M., 2015. Fluid lipid membranes: From differential geometry to curvature stresses. Chemistry and physics of lipids 185:11–45.

30. Smith, A.-S., E. Sackmann, and U. Seifert, 2004. Pulling tethers from adhered vesicles. Physical review letters 92:208101.

31. Roux, A., G. Cappello, J. Cartaud, J. Prost, B. Goud, and P. Bassereau, 2002. A minimal system allowing tubulation with molecular motors pulling on giant liposomes. Proceedings of the National Academy of Sciences 99:5394–5399.

32. Waugh, R. E., 1982. Surface viscosity measurements from large bilayer vesicle tether formation. II. Experiments. Biophysical journal 38:29–37.

33. Heinrich, V., B. Božič, S. Svetina, and B. Žekš, 1999. Vesicle deformation by an axial load: from elongated shapes to tethered vesicles. Biophysical journal 76:2056–2071.

34. Derényi, I., F. Jülicher, and J. Prost, 2002. Formation and interaction of membrane tubes. Physical review letters 88:238101.

35. Powers, T. R., G. Huber, and R. E. Goldstein, 2002. Fluid-membrane tethers: minimal surfaces and elastic boundary layers. Physical Review E 65:041901.

36. Dmitrieff, S., and F. Nédélec, 2015. Membrane mechanics of endocytosis in cells with turgor. PLoS computational biology 11:e1004538.

37. Seifert, U., 1997. Configurations of fluid membranes and vesicles. Advances in Physics 46:13–137. http://dx.doi.org/10.1080/00018739700101488.

38. Buehrle, J., S. Herminghaus, and F. Mugele, 2002. Impact of line tension on the equilibrium shape of liquid droplets on patterned substrates. Langmuir 18:9771–9777.

39. Richmond, D. L., E. M. Schmid, S. Martens, J. C. Stachowiak, N. Liska, and D. A. Fletcher, 2011. Forming giant vesicles with controlled membrane composition, asymmetry, and contents. Proceedings of the National Academy of Sciences 108:9431–9436.

40. Agrawal, A., and D. J. Steigmann, 2009. Modeling protein-mediated morphology in biomembranes. Biomechanics and modeling in mechanobiology 8:371–379.

41. Liu, J., M. Kaksonen, D. G. Drubin, and G. Oster, 2006. Endocytic vesicle scission by lipid phase boundary forces. Proceedings of the National Academy of Sciences 103:10277–10282.

42. Dan, N., and S. Safran, 1998. Effect of lipid characteristics on the structure of transmembrane proteins. Biophysical Journal 75:1410–1414.

43. Lipowsky, R., 1992. Budding of membranes induced by intramembrane domains. Journal de Physique II 2:1825–1840.

44. Pontes, B., Y. Ayala, A. C. C. Fonseca, L. F. Romão, R. F. Amaral, L. T. Salgado, F. R. Lima, M. Farina, N. B. Viana, V. Moura-Neto, et al., 2013. Membrane elastic properties and cell function. PLoS One 8:e67708.

45. Bouissou, A., A. Proag, N. Bourg, K. Pingris, C. Cabriel, S. Balor, T. Mangeat, C. Thibault, C. Vieu, G. Dupuis, et al., 2017. Podosome Force Generation Machinery: A Local Balance between Protrusion at the Core and Traction at the Ring. ACS nano 11:4028–4040.

46. Proag, A., A. Bouissou, T. Mangeat, R. Voituriez, P. Delobelle, C. Thibault, C. Vieu, I. Maridonneau-Parini, and R. Poincloux, 2015. Working together: spatial synchrony in the force and actin dynamics of podosome first neighbors. ACS nano 9:3800–3813.

47. Linder, S., 2009. Invadosomes at a glance. J Cell Sci 122:3009–3013.

48. Labernadie, A., C. Thibault, C. Vieu, I. Maridonneau-Parini, and G. M. Charrière, 2010. Dynamics of podosome stiffness revealed by atomic force microscopy. Proceedings of the National Academy of Sciences 107:21016–21021.

49. Kronenberg, N. M., P. Liehm, A. Steude, J. A. Knipper, J. G. Borger, G. Scarcelli, K. Franze, S. J. Powis, and M. C. Gather, 2017. Long-Term Imaging of Cellular Forces with High Precision by Elastic Resonator Interference Stress Microscopy. bioRxiv 118554.

50. Timoshenko, S. P., and S. Woinowsky-Krieger, 1959. Theory of plates and shells. McGraw-hill.

51. Avinoam, O., M. Schorb, C. J. Beese, J. A. Briggs, and M. Kaksonen, 2015. Endocytic sites mature by continuous bending and remodeling of the clathrin coat. Science 348:1369–1372.

52. McCullough, J., A. K. Clippinger, N. Talledge, M. L. Skowyra, M. G. Saunders, T. V. Naismith, L. A. Colf, P. Afonine, C. Arthur, W. I. Sundquist, et al., 2015. Structure and membrane remodeling activity of ESCRT-III helical polymers. Science 350:1548–1551.

53. Baumgart, T., B. R. Capraro, C. Zhu, and S. L. Das, 2011. Thermodynamics and mechanics of membrane curvature generation and sensing by proteins and lipids. Annual review of physical chemistry 62:483–506.

54. Stachowiak, J. C., F. M. Brodsky, and E. A. Miller, 2013. A cost-benefit analysis of the physical mechanisms of membrane curvature. Nature cell biology 15:1019–1027.

55. Dannhauser, P. N., and E. J. Ungewickell, 2012. Reconstitution of clathrin-coated bud and vesicle formation with minimal components. Nature Cell Biology 14:634–639.

56. Frost, A., V. M. Unger, and P. De Camilli, 2009. The BAR domain superfamily: membrane-molding macromolecules. Cell 137:191–196.

57. Chan, Y.-H. M., and S. G. Boxer, 2007. Model membrane systems and their applications. Current opinion in chemical biology 11:581–587.

58. Ayton, G. S., W. G. Noid, and G. A. Voth, 2007. Multiscale modeling of biomolecular systems: in serial and in parallel. Current opinion in structural biology 17:192–198.

59. Lee, H., and R. W. Pastor, 2011. Coarse-grained model for PEGylated lipids: effect of PEGylation on the size and shape of self-assembled structures. The Journal of Physical Chemistry B 115:7830–7837.

60. Lim, S. K., A. S. Wong, H.-P. M. de Hoog, P. Rangamani, A. N. Parikh, M. Nallani, S. Sandin, and B. Liedberg, 2017. Spontaneous formation of nanometer scale tubular vesicles in aqueous mixtures of lipid and block copolymer amphiphiles. Soft Matter .

Supplementary material for "The role of traction in membrane curvature generation"

Haleh Alimohamadi [1+], Ritvik Vasan[1+], Julian E. Hassinger[2], Jeanne.C. Stachowiak[3], Padmini Rangamani[1*]

[1]Department of Mechanical and Aerospace Engineering, University of California San Diego, La Jolla, CA 92093; [2]Biophysics Graduate Group, University of California Berkeley, Berkeley, CA 94720
[3]Department of Biomedical Engineering, University of Texas at Austin, Austin, TX 78712
*Corresponding author: prangamani@ucsd.edu
[+]These authors contributed equally to this work

Contents

1 Model Development **2**
1.1 Assumptions . . . 2
1.2 Equilibrium equations . . . 2
1.3 Helfrich energy with constant bending and Gaussian moduli . . . 3
1.4 Helfrich energy with variable bending and Gaussian moduli . . . 4
1.5 Axisymmetric coordinates . . . 4
1.5.1 Equation of motion for constant bending and Gaussian moduli . . . 4
1.5.2 Equation of motion for variable bending and Gaussian moduli . . . 6
1.5.3 Force balance along the membrane for constant bending and Gaussian moduli . . . 6
1.5.4 Force balance along the membrane for variable bending and Gaussian moduli . . . 7
1.6 1D Monge particularization . . . 8
1.7 Asymptotic approximation for small radius . . . 9

2 Image analysis **12**

3 Table of notation **14**

4 Additional tether and bud formation simulations **16**
4.1 Tubes pulled against surface tension . . . 16
4.2 Tubes pulled against pressure . . . 16
4.3 Tubes pulled against pressure and surface tension . . . 17
4.4 Axial and radial tractions in bud formation . . . 20
4.5 Bud formation in heterogeneous membrane with negative surface tension at boundary . . . 21
4.6 Surface tension at the boundary regulates line tension at interface . . . 22

5 Podosome protrusion simulation **22**

6 Additional images of vesicle with phase separation **22**

1 Model Development

1.1 Assumptions

- Membrane curvature generated due to forces or protein-induced spontaneous curvature is much larger than the thickness of the bilayer. Based on this assumption, we model the lipid bilayer as a thin elastic shell with a bending energy given by the Helfrich-Canham energy, which is valid for radii of curvatures much larger than the thickness of the bilayer [1, 2].
- We neglect the surrounding fluid flow or inertial dynamics and assume that the membrane is at mechanical equilibrium at all times [3]. This assumption is commonly used in the modeling of membrane curvature to keep the mathematics tractable [4].
- The membrane is incompressible because the energetic cost of stretching the membrane is high [5]. This constraint is implemented using a Lagrange multiplier [6, 7] as discussed in Section 1.2.
- Finally, for simplicity in the numerical simulations, we assume that the membrane in the region of interest is either rotationally symmetric (Fig. 1) or the out-of-plane membrane deformation is small and we can parametrize our system by a 1D Monge gauge.

1.2 Equilibrium equations

Force balance on the membrane can be written as

$$\nabla \cdot \boldsymbol{\sigma} + p\mathbf{n} = \mathbf{f}, \tag{S1}$$

where $\nabla\cdot$ is surface divergence, $\boldsymbol{\sigma}$ is the stress vector, p is the pressure difference between the inside and outside of the volume bounded by the membrane, and $\mathbf{f}$ is any externally applied force per unit area on the membrane. By introducing the covariant derivative as $()_{;\alpha}$, the surface divergence in Eq. S1 can be rewritten as [4]

$$\nabla \cdot \boldsymbol{\sigma} = \boldsymbol{\sigma}^{\alpha}_{;\alpha} = (\sqrt{a})^{-1}(\sqrt{a}\boldsymbol{\sigma}^{\alpha})_{,\alpha}, \tag{S2}$$

where a is the determinant of the first fundamental form metric $a_{\alpha\beta}$. The surface stresses in Eq. S1 can be split into normal and tangential component given by

$$\sigma^{\alpha} = T^{\alpha} + S^{\alpha}\mathbf{n}, \tag{S3}$$

where

$$\mathbf{T}^{\alpha} = T^{\alpha\beta}\mathbf{a}_{\beta}, \qquad T^{\alpha\beta} = \sigma^{\alpha\beta} + b^{\beta}_{\mu}M^{\mu\alpha}, \qquad S^{\alpha} = -M^{\alpha\beta}_{;\beta}. \tag{S4}$$

The two tensors $\sigma^{\alpha\beta}$ and $M^{\alpha\beta}$ can be expressed by the derivative of F, the energy per unit mass, with respect to the coefficients of the first and second fundamental forms, $a_{\alpha\beta}$, $b_{\alpha\beta}$, respectively [4, 6]

$$\sigma^{\alpha\beta} = \rho\left(\frac{\partial F(\rho, H, K; x^{\alpha})}{\partial a_{\alpha\beta}} + \frac{\partial F(\rho, H, K; x^{\alpha})}{\partial a_{\beta\alpha}}\right), \quad M^{\alpha\beta} = \frac{\rho}{2}\left(\frac{\partial F(\rho, H, K; x^{\alpha})}{\partial b_{\alpha\beta}} + \frac{\partial F(\rho, H, K; x^{\alpha})}{\partial b_{\beta\alpha}}\right), \tag{S5}$$

where ρ is the surface mass density. H and K are mean and Gaussian curvatures given by

$$H = \frac{1}{2}a^{\alpha\beta}b_{\alpha\beta}, \quad K = \frac{1}{2}\varepsilon^{\alpha\beta}\varepsilon^{\lambda\mu}b_{\alpha\lambda}b_{\beta\mu}. \tag{S6}$$

Here $(a^{\alpha\beta}) = (a_{\alpha\beta})$ is the dual metric and $\varepsilon^{\alpha\beta}$ is the permutation tensor defined by $\varepsilon^{12} = -\varepsilon^{21} = \frac{1}{\sqrt{a}}, \varepsilon^{11} = \varepsilon^{22} = 0$.

The area incompressibility ($J = 1$) constraint is implemented using a general form of free energy density per unit mass given as

$$F(\rho, H, K; x^\alpha) = \tilde{F}(H, K; x^\alpha) - \frac{\gamma(x^\alpha, t)}{\rho}. \tag{S7}$$

Here $\gamma(x^\alpha, t)$ is a Lagrange multiplier field required to impose invariance of ρ on the whole of the surface (see [4] for full derivation). Substituting $W = \rho\tilde{F}$ into Eq. S7 we get

$$\sigma^{\alpha\beta} = (\lambda + W)a^{\alpha\beta} - (2HW_H + 2\kappa W_K)a^{\alpha\beta} + W_H\tilde{b}^{\alpha\beta}, \tag{S8}$$

$$M^{\alpha\beta} = \frac{1}{2}W_H a^{\alpha\beta} + W_K\tilde{b}^{\alpha\beta}, \tag{S9}$$

where

$$\lambda = -(\gamma + W). \tag{S10}$$

Combining Eqs. S9, S4, and S3 into Eq. S1 gives the equations in normal and tangential equations as

$$p + \mathbf{f}\cdot\mathbf{n} = \Delta\frac{1}{2}W_H + (W_K)_{;\alpha\beta}\tilde{b}^{\alpha\beta} + W_H(2H^2 - K) + 2H(KW_K - W) - 2\lambda H, \tag{S11}$$

and

$$N^{\beta\alpha}_{;\alpha} - S^\alpha b^\beta_\alpha = -(\gamma_{,\alpha} + W_K k_{,\alpha} + W_H H_{,\alpha})a^{\beta\alpha} = (\frac{\partial W}{\partial x^\alpha_{|exp}} + \lambda_{,\alpha})a^{\beta\alpha} = \mathbf{f}.\mathbf{a}_s. \tag{S12}$$

Here $\Delta(\cdot)$ is the surface Laplacian and $()_{|exp}$ denotes the explicit derivative respect to coordinate θ^α.

1.3 Helfrich energy with constant bending and Gaussian moduli

For a lipid bilayer with uniform bending and Gaussian moduli, we use a modified version of the Helfrich energy to account for the spatial variation of spontaneous curvature [7–9],

$$W = \kappa(H - C(\theta^\alpha))^2 + \kappa_G K, \tag{S13}$$

where W is the local energy density, C is the spontaneous curvature, and κ (bending modulus) and κ_G (Gaussian modulus) are constant. It should be mentioned that Eq. S13 is different from the standard Helfrich energy by a factor of 2. We take this net effect into consideration by choosing the value of the bending modulus to be twice that of the standard value of bending modulus typically used for lipid bilayers [1]. Though the membrane bending and Gaussian moduli need not necessarily be uniform due to composition variation along the membrane [10, 11], assuming uniform κ and κ_G is an acceptable simplification for classical simulations. In both the tube and bud simulations, we assumed that bending and Gaussian moduli are constants. The general form of the following equations with variable bending and Gaussian moduli is given in Section 1.4.

At equilibrium, the integration of local energy density over the total membrane surface area ω gives the strain energy of the system written as

$$E = \int_\omega (\kappa(H - C(\theta^\alpha))^2 + \kappa_G K)da, \tag{S14}$$

where E is total strain energy. Imposing area and volume constrains by Lagrange multipliers p (pressure) and λ (surface tension) gives

$$E = \int_\omega \underbrace{(\kappa(H - C(\theta^\alpha))^2 + \kappa_G K + \lambda)}_{\text{Energy density}} da - \underbrace{pV(\omega)}_{\text{Pressure work}} , \tag{S15}$$

where V is the volume associated with the membrane surface. The strain energy in Eq. S15 can be split into three different components as

$$E = \underbrace{\int_\omega (\kappa(H - C(\theta^\alpha)^2 + \kappa_G K) da}_{\text{Bending energy}} + \underbrace{\int_\omega \lambda da}_{\text{Surface tension work}} - \underbrace{pV(\omega)}_{\text{Pressure work}} . \tag{S16}$$

Using the Helfrich energy function Eq. S13, in the balance of forces normal to the membrane (Eq. S11) yields the "shape equation,"

$$\underbrace{\kappa \Delta \left[(H - C)\right] + 2\kappa \left(H - C\right) \left(2H^2 - K\right) - 2\kappa H \left(H - C\right)^2}_{\text{Elastic Effects}} = \underbrace{p + 2\lambda H}_{\text{Capillary effects}} + \underbrace{\mathbf{f} \cdot \mathbf{n}}_{\text{Force due to actin}} , \tag{S17}$$

where λ can be interpreted to be the membrane tension [7].

A consequence of heterogeneous protein-induced spontaneous curvature, heterogeneous moduli, and externally applied force is that λ is not homogeneous along the membrane [7, 8, 12]. Substituting Eq. S13 into the balance of forces tangent to the membrane Eq. S12 gives the spatial variation of membrane tension,

$$\underbrace{\lambda_{,\alpha}}_{\substack{\text{Gradient of}\\ \text{surface tension}}} = \underbrace{2\kappa \left(H - C\right) \frac{\partial C}{\partial \theta^\alpha}}_{\text{Protein-induced variation}} - \underbrace{\mathbf{f} \cdot \mathbf{a}_\alpha}_{\substack{\text{Force induced}\\ \text{variation}}} . \tag{S18}$$

1.4 Helfrich energy with variable bending and Gaussian moduli

For a membrane with variable bending and Gaussian moduli the modified Helfrich energy in Eq. S13 becomes

$$W = \kappa(\theta^\alpha)(H - C(\theta^\alpha))^2 + \kappa_G(\theta^\alpha) K, \tag{S19}$$

where both moduli vary along the membrane. Substituting Eq. S19 into Eqs. S17 and S18 gives a complete form of the so-called "shape equation" and spatial variation of membrane tension:

$$\Delta \left[\kappa \left(H - C\right)\right] + 2H\Delta\kappa_G - (\kappa_G)_{;\alpha\beta} b^{\alpha\beta} + 2\kappa \left(H - C\right) \left(2H^2 - K\right) - 2\kappa H \left(H - C\right)^2 = p + 2\lambda H + \mathbf{f} \cdot \mathbf{n}, \tag{S20}$$

$$\lambda_{,\alpha} = 2\kappa \left(H - C\right) \frac{\partial C}{\partial \theta^\alpha} - \frac{\partial \kappa}{\partial \theta^\alpha} (H - C)^2 - \frac{\partial \kappa_G}{\partial \theta^\alpha} K - \mathbf{f} \cdot \mathbf{a}_\alpha. \tag{S21}$$

Here, $b^{\alpha\beta}$ are components of the curvature tensor.

1.5 Axisymmetric coordinates

1.5.1 Equation of motion for constant bending and Gaussian moduli

We parameterize a surface of revolution (Fig. 1B) by

$$\mathbf{r}(s, \theta) = r(s)\mathbf{e}_r(\theta) + z(s)\mathbf{k}. \tag{S22}$$

We define ψ as the angle made by the tangent with respect to the horizontal. This gives $r'(s) = \cos(\psi)$, $z'(s) = \sin(\psi)$, which satisfies the identity $(r')^2 + (z')^2 = 1$. Using this, we define the normal to the surface as $\mathbf{n} = -\sin\psi\mathbf{e}_r(\theta) + \cos\psi\mathbf{k}$, the tangent to the surface in the direction of increasing arc length as $\boldsymbol{\nu} = \cos\psi\mathbf{e}_r(\theta) + \sin\psi\mathbf{k}$, and unit vector $\boldsymbol{\tau} = \mathbf{e}_\theta$ tangent to the boundary $\partial\omega$ in the direction of the surface of revolution (see Fig. 1B).

This parameterization yields the following expressions for tangential (κ_ν) and transverse (κ_τ) curvatures, and twist (τ):

$$\kappa_\nu = \psi^{'}, \quad \kappa_\tau = r^{-1}\sin\psi, \quad \tau = 0. \tag{S23}$$

The mean curvature (H) and Gaussian curvature (K) are obtained by summation and multiplication of the tangential and transverse curvatures

$$H = \frac{1}{2}(\kappa_\nu + \kappa_\tau) = \frac{1}{2}(\psi^{'} + r^{-1}\sin\psi), \quad K = \kappa_\tau\kappa_\nu = \frac{\psi^{'}\sin\psi}{r}. \tag{S24}$$

Defining $L = \frac{1}{2\kappa}r(W_H)'$, we write the system of first order differential equations governing the problem as [12],

$$\begin{gathered} r' = \cos\psi, \quad z' = \sin\psi, \quad r\psi' = 2rH - \sin\psi, \quad rH' = L + rC', \\ \frac{L'}{r} = \frac{p}{k} + \frac{\mathbf{f}\cdot\mathbf{n}}{\kappa} + 2H\left[(H-C)^2 + \frac{\lambda}{\kappa}\right] - 2\left(H-C\right)\left[H^2 + \left(H - r^{-1}\sin\psi\right)^2\right], \\ \lambda' = 2\kappa\left(H-C\right)C' - \mathbf{f}\cdot\mathbf{a_s}. \end{gathered} \tag{S25}$$

The applied boundary conditions are

$$\begin{gathered} r(0^+) = 0, \quad L(0^+) = 0, \quad \psi(0^+) = 0, \\ z(s_{max}) = 0, \quad \psi(s_{max}) = 0, \quad \lambda(s_{max}) = \lambda_0. \end{gathered} \tag{S26}$$

In asymmetric coordinates, the manifold area can be expressed in term of arc length [12]

$$a(s) = 2\pi\int_0^s r(\xi)d\xi \quad \rightarrow \quad \frac{da}{ds} = 2\pi r. \tag{S27}$$

Eq. S27 allows us to convert Eq. S25 to an area derivative and prescribe the total area of the membrane.

We non-dimensionalized the system of equations as

$$\begin{gathered} \zeta = \frac{a}{2\pi R_0^2}, \quad x = \frac{r}{R_0}, \quad y = \frac{y}{R_0}, \quad h = HR_0, \quad c = CR_0, \quad l = LR_0, \\ \lambda^* = \frac{\lambda R_0^2}{\kappa_0}, \quad p^* = \frac{pR_0^3}{\kappa_0}, \quad f^* = \frac{fR_0^3}{\kappa_0}, \quad \kappa^* = \frac{\kappa}{\kappa_0}, \end{gathered} \tag{S28}$$

where R_0 is the radius of the initially circular membrane patch.

Rewriting Eq. S25 in terms of Eq. S27 and the dimensionless variables Eq. S28, we get [12]

$$\begin{gathered} x\dot{x} = \cos\psi, \quad x\dot{y} = \sin\psi, \quad x^2\dot{\psi} = 2xh - \sin\psi, \quad x^2\dot{h} = l + x^2\dot{c}, \\ \dot{l} = \frac{p^*}{\kappa^*} + \frac{\mathbf{f}^*\cdot\mathbf{n}}{\kappa^*} + 2h\left[(h-c)^2 + \frac{\lambda^*}{\kappa^*}\right] - 2\left(h-c\right)\left[h^2 + \left(h - x^{-1}\sin\psi\right)^2\right], \\ \dot{\lambda^*} = 2\kappa^*\left(h-c\right)\dot{c} - \frac{\mathbf{f}^*\cdot\mathbf{a_s}}{x}. \end{gathered} \tag{S29}$$

The spontaneous curvature field is modeled by a hyperbolic tangent functional as

$$C = \frac{1}{2}[\tanh(g(\zeta - a_0))], \tag{S30}$$

where a_0 is the area of applied spontaneous curvature and $g = 20$ is a constant that ensures a sharp but smooth transition.

1.5.2 Equation of motion for variable bending and Gaussian moduli

For a non-uniform membrane with variable bending and Gaussian moduli, the governing system of equations in Eq. S25 becomes

$$\begin{aligned} r' = \cos\psi, \quad z' = \sin\psi, \quad r\psi' = 2rH - \sin\psi, \\ rH' = L + rC' - \frac{r\kappa'}{\kappa}(H - C), \quad \lambda' = 2\kappa\,(H - C)\,C' - \mathbf{f}\cdot\mathbf{a_s}, \\ \frac{L'}{r} = \frac{p}{k} + \frac{\mathbf{f}\cdot\mathbf{n}}{\kappa} + 2H\left[(H-C)^2 + \frac{\lambda}{\kappa}\right] - 2\,(H-C)\left[H^2 + \left(H - r^{-1}\sin\psi\right)^2\right] \\ -\frac{\kappa'}{\kappa}\frac{L}{r} - \frac{\kappa_G''}{\kappa}\frac{\sin\psi}{r} - \frac{\kappa_G'}{\kappa}\frac{\cos\psi}{r}(2H - \frac{\sin\psi}{r}). \end{aligned} \tag{S31}$$

The applied boundary conditions are the same as Eq. S26. In addition to Eq. S28, we define two additional terms:

$$\kappa_G^* = \frac{\kappa_G}{\kappa_0}, \quad \text{and} \quad K^* = KR_0^2. \tag{S32}$$

The non-dimensional system of equations in Eq. S29 becomes

$$\begin{aligned} x\dot{x} = \cos\psi, \quad x\dot{y} = \sin\psi \quad x^2\dot{\psi} = 2xh - \sin\psi, \quad x^2\dot{h} = l + x^2\dot{c} - x^2\frac{\dot{\kappa^*}}{\kappa^*}(h-c) \\ \dot{l} = \frac{p^*}{\kappa^*} + \frac{\mathbf{f}^*\cdot\mathbf{n}}{\kappa^*} + 2h\left[(h-c)^2 + \frac{\lambda^*}{\kappa^*}\right] - 2\,(h-c)\left[h^2 + \left(h - x^{-1}\sin\psi\right)^2\right] \\ -\frac{\dot{\kappa^*}}{\kappa^*}l - x\frac{\ddot{\kappa}_G^*}{\kappa^*}\sin\psi - \frac{\dot{\kappa}_G^*}{\kappa}\cos\psi(2h - \frac{\sin\psi}{x}), \\ \dot{\lambda^*} = 2\kappa^*\,(h-c)\,\dot{c} - \dot{\kappa^*}(h-c)^2\dot{c} - \dot{\kappa}_G^* K^* - \frac{\mathbf{f}^*\cdot\mathbf{a_s}}{x}. \end{aligned} \tag{S33}$$

1.5.3 Force balance along the membrane for constant bending and Gaussian moduli

A general force balance for a surface ω, bounded by a curve $\partial\omega$, is (Fig. 1B)

$$\int_\omega p\mathbf{n}da + \int_{\partial\omega}\tilde{\mathbf{f}}dt + \mathbf{F} = 0, \tag{S34}$$

where $t = r(s)\theta$ is the length along the curve of revolution perimeter, p is the pressure difference across the membrane, $\tilde{\mathbf{f}}$ is the traction along the curve of revolution t and $\mathbf{F}$ is any externally applied force on the membrane. Along any circumferential curve on the membrane at constant z, the traction is given by [6, 8]

$$\tilde{\mathbf{f}} = \tilde{f}_\nu\boldsymbol{\nu} + \tilde{f}_n\mathbf{n} + \tilde{f}_\tau\boldsymbol{\tau}, \tag{S35}$$

where

$$\begin{aligned} \tilde{f}_n = (\tau W_K)' - 1/2(W_H)_{,\nu} - (W_K)_{,\beta}\tilde{b}^{\alpha\beta}\nu_\alpha, \\ \tilde{f}_\nu = W + \lambda - \kappa_\nu M, \\ \tilde{f}_\tau = -\tau M, \end{aligned} \tag{S36}$$

and $\tilde{f}_n$, $\tilde{f}_\nu$ and $\tilde{f}_\tau$ are force per unit length acting along the normal $\mathbf{n}$, tangent $\boldsymbol{\nu}$ to the surface, and transverse tangent $\mathbf{e}_\theta$ respectively. In Eq. S36, M is the bending couple given by

$$M = \frac{1}{2}W_H + \kappa_\nu W_K. \tag{S37}$$

Because $\tau = 0$ (no twist) in asymmetric coordinates, the normal and tangential tractions become

$$\tilde{f}_n = -\kappa(H' - C'), \tag{S38a}$$

$$\tilde{f}_\nu = \kappa(H - C)(H - C - \psi') + \lambda. \tag{S38b}$$

Projecting Eq. S35 onto the orthogonal bases $\mathbf{e}_r$ and $\mathbf{k}$ gives us the equation for axial and radial tractions [6, 8],

$$\tilde{f}_r = \underbrace{\kappa(H' - C')\sin\psi}_{\substack{\text{Curvature gradient}\\ \text{contribution}}} + \underbrace{\kappa(H - C)(H - C - \psi')\cos\psi}_{\substack{\text{Curvature}\\ \text{contribution}}} + \underbrace{\lambda\cos\psi}_{\substack{\text{Tension}\\ \text{contribution}}}, \tag{S39a}$$

$$\tilde{f}_z = \underbrace{-\kappa(H' - C')\cos\psi}_{\substack{\text{Curvature gradient}\\ \text{contribution}}} + \underbrace{\kappa(H - C)(H - C - \psi')\sin\psi}_{\substack{\text{Curvature}\\ \text{contribution}}} + \underbrace{\lambda\sin\psi}_{\substack{\text{Tension}\\ \text{contribution}}}. \tag{S39b}$$

Because $\int_{\partial\omega} dt = 2\pi r$, the applied force in the axial direction can be evaluated by substituting Eqs. S39a,and S39b into Eq. S34,

$$-\mathbf{F}_z = \underbrace{2\pi r\left(-\kappa(H' - C')\cos\psi\right) + \kappa(H - C)(H - C - \psi')\sin\psi + \lambda\sin\psi}_{\text{Force due to traction}} + \underbrace{2\pi\int_0^s pr(\xi)\cos\psi d\xi}_{\text{Force due to pressure}}. \tag{S40}$$

This can be rewritten in terms of tractions as

$$-\mathbf{f}_z = \underbrace{\left(-\kappa(H' - C')\cos\psi\right) + \kappa(H - C)(H - C - \psi')\sin\psi + \lambda\sin\psi}_{\text{axial traction}} + \underbrace{\frac{\int_0^s pr(\xi)\cos\psi d\xi}{r}}_{\text{Traction due to pressure}}, \tag{S41}$$

where $\mathbf{f}_z = \frac{\mathbf{F}_z}{2\pi r}$. The energy per unit length ξ, or "effective line tension," can be found by integrating Eq. S39a along the perimeter boundary $\partial\omega$,

$$\xi = 2\pi r\Big[\underbrace{\kappa(H - C)(H - C - \psi')\cos\psi}_{\substack{\text{Curvature}\\ \text{contribution}}} + \underbrace{\lambda\cos\psi}_{\substack{\text{Tension}\\ \text{contribution}}} + \underbrace{\kappa(H' - C')\sin\psi}_{\substack{\text{Curvature gradient}\\ \text{contribution}}}\Big]. \tag{S42a}$$

1.5.4 Force balance along the membrane for variable bending and Gaussian moduli

For a membrane with variable bending moduli, the normal and tangential tractions in Eqs. S38a, S38b become

$$\tilde{f}_n = -\kappa(H' - C') - \kappa'(H - C) - \frac{\sin\psi}{r}\kappa'_G, \tag{S43a}$$

$$\tilde{f}_\nu = \kappa(H - C)(H - C - \psi') + \lambda. \tag{S43b}$$

The radial and axial tractions in Eqs. S39a and S39b can be rewritten for the general case as

$$\begin{aligned}\tilde{f}_r = {} & \kappa(H' - C')\sin\psi + \kappa(H - C)(H - C - \psi')\cos\psi + \lambda\cos\psi \\ & + \underbrace{\kappa'(H - C)\sin\psi}_{\substack{\text{Variable bending}\\ \text{modulus}}} + \underbrace{\frac{\sin\psi^2}{r}\kappa'_G}_{\substack{\text{Variable Gaussian}\\ \text{modulus}}},\end{aligned} \tag{S44a}$$

$$\begin{aligned}\tilde{f}_z = {} & -\kappa(H' - C')\cos\psi + \kappa(H - C)(H - C - \psi')\sin\psi + \lambda\sin\psi \\ & - \underbrace{\kappa'(H - C)\cos\psi}_{\substack{\text{Variable bending}\\ \text{modulus}}} - \underbrace{\frac{\sin\psi\cos\psi}{r}\kappa'_G}_{\substack{\text{Variable Gaussian}\\ \text{modulus}}}.\end{aligned} \tag{S44b}$$

Similarly, the axial force and energy per unit lengths in Eqs. S40, S42a can be rewritten as

$$\mathbf{F}_z = \Big[\underbrace{2\pi r(-\kappa(H'-C')\cos\psi + \kappa(H-C)(H-C-\psi')\sin\psi + \lambda\sin\psi - \kappa'(H-C)\cos\psi - \frac{\sin\psi\cos\psi}{r}\kappa'_G)}_{\text{Force due to traction}}\Big] + \underbrace{2\pi\int_0^s pr(\xi)\cos\psi d\xi}_{\text{Force due to pressure}}, \tag{S45a}$$

$$\xi = 2\pi r\Big[\underbrace{\kappa(H-C)(H-C-\psi')\cos\psi}_{\text{Curvature contribution}} + \underbrace{\lambda\cos\psi}_{\text{Tension contribution}} + \underbrace{\kappa(H'-C')\sin\psi}_{\text{Curvature gradient contribution}} - \underbrace{\kappa'(H-C)\sin\psi}_{\text{Variable bending contribution}} - \underbrace{\frac{\sin\psi^2}{r}\kappa'_G}_{\text{Variable Gaussian contribution}}\Big]. \tag{S46a}$$

1.6 1D Monge particularization

For small deformations of the membrane (i.e. $\ll$ than the "natural length scale" of the membrane $\sim \sqrt{\kappa/\lambda}$ [13]) a 1D Monge particularization is the most straightforward parametrization of the membrane surface. Given any point x on the plane $z = 0$, the membrane has some height z. Thus, the position of a point on the membrane is given by

$$\mathbf{r}(x) = x\mathbf{e}_1 + z(x)\mathbf{e}_3, \tag{S47}$$

where ($\mathbf{e}_1$, $\mathbf{e}_3$) are the unit vectors in 'x' and 'z' directions. Assuming a small deformation ($z_{,x} \ll 1$) the normal and tangential vectors to the surface are defined as

$$\mathbf{n} = -z_{,x}\mathbf{e}_1 + 1\mathbf{e}_3, \tag{S48a}$$

$$\boldsymbol{\nu} = -1\mathbf{e}_1 + z_{,x}\mathbf{e}_3. \tag{S48b}$$

And the mean and Gaussian curvatures are [14]

$$2H = z_{,xx}, \quad K = 0. \tag{S49}$$

Along any boundary curve, traction is given by its two components as

$$\tilde{\mathbf{f}} = \tilde{f}_\nu\boldsymbol{\nu} + \tilde{f}_n\mathbf{n}, \tag{S50}$$

where normal and tangential tractions are simplified as [15]

$$\tilde{f}_n = -\kappa(H'-C'), \tag{S51a}$$

$$\tilde{f}_\nu = \kappa(H-C)(H-C-H_{,xx}) + \lambda. \tag{S51b}$$

Projecting Eq. S50 into the axial direction $\mathbf{e}_3$ gives us

$$\tilde{f}_z = (\kappa(H-C)(H-C-H_{,xx}) + \lambda)z_{,x} - \kappa(H'-C'). \tag{S52}$$

Assuming that any cut through the center of a membrane protrusion (e.g. podosomes) gives us the same 1D curve, we can calculate the axial force by taking the contour integral of axial traction in Eq. S52,

$$-\mathbf{F}_z = \pi D\left((\kappa(H-C)(H-C-H_{,xx}) + \lambda)z_{,x} - \kappa(H'-C')\right), \tag{S53}$$

where D is the largest diameter of the cut curve at the base.

1.7 Asymptotic approximation for small radius

To ensure continuity at the poles, we use $L = H' = 0$ as a boundary condition in our simulations. However, this boundary condition reduces the expressions for tractions (Eqs. S39b, S39a) to zero at the pole. To avoid this discrepancy, we derive an asymptotic expression for tractions at small arc length. We proceed by assuming that the pole in Eq. S29 is at $x = 0$ and choose a rescaled variable given by

$$X = \frac{x}{\epsilon}. \tag{S54}$$

Here, ϵ is a small parameter, so that X is order of one. We can extend this to other small variables in Eq. S29 near the pole to get

$$y = y_0 + Y\epsilon, \quad \psi = P\epsilon, \quad s = S\epsilon, \tag{S55}$$

where Y, P, S are the corresponding rescaled parameters and y_0 is membrane height at the pole.

In the simple case with no spontaneous curvature ($C = 0$), no external force $\mathbf{f} = 0$ and no pressure difference $p = 0$, we substitute Eqs. S55 and S54 into Eq. S29 and use a Taylor expansion to get

$$\begin{aligned} \dot{X} = 1 - \frac{(P\epsilon)^2}{2}, \quad \dot{Y} = P\epsilon - \frac{(P\epsilon)^3}{3!}, \quad \dot{P} = 2h - \frac{P}{X} + \frac{\epsilon^2}{3!}\frac{P^3}{X}, \quad X\dot{h} = l, \\ \dot{l} = \epsilon^2 2Xh\left[\frac{\lambda^*}{k^*} - \left(h - \frac{P}{X} + \frac{P^3\epsilon^2}{X3!}\right)^2\right], \\ \dot{\lambda^*} = 0. \end{aligned} \tag{S56}$$

We look for a solutions with form of

$$\begin{aligned} h = h^0 + \epsilon h^1 + \mathrm{ord}(\epsilon^2), \quad X = X^0 + \epsilon X^1 + \mathrm{ord}(\epsilon^2), \quad Y = Y^0 + \epsilon Y^1 + \mathrm{ord}(\epsilon^2), \\ l = l^0 + \epsilon l^1 + \mathrm{ord}(\epsilon^2), \quad P = P^0 + \epsilon P^1 + \mathrm{ord}(\epsilon^2), \quad \lambda^* = \lambda^{*0} + \epsilon\lambda^{*1} + \mathrm{ord}(\epsilon^2). \end{aligned} \tag{S57}$$

The leading order terms in Eq. S57 are

$$\dot{X^0} = 1, \quad \dot{Y^0} = 0, \quad \dot{P^0} = 2h^0 - \frac{P^0}{X^0}, \quad \dot{h^0} = \frac{l^0}{X^0}, \quad \dot{l^0} = 0, \quad \dot{\lambda}^{*0} = 0. \tag{S58}$$

Integrating the differential equations in Eq. S58, we get

$$\begin{aligned} X^0 = S, \quad Y^{*0} = Y_0, \quad P^0 = S\left(H_0 + L_0\log(S) - \frac{L_0}{2}\right), \\ h^0 = L_0\log(S) + H_0, \quad l^0 = L_0, \quad \lambda^0 = \lambda_0, \end{aligned} \tag{S59}$$

where Y_0, H_0 and L_0, λ_0 are integration constants. We then look at order ϵ^1 terms in Eq. S56

$$\dot{X^1} = 0, \quad \dot{Y^1} = P, \quad \dot{P^1} = 2h^1 + \frac{P^0X^1}{{X^0}^2}, \quad X^0\dot{h^1} + X^1\dot{h^0} = l^1, \quad \dot{l^1} = 0, \quad \dot{\lambda}^{*1} = 0. \tag{S60}$$

The first order terms are thus given by

$$\begin{aligned} X^1 = X_1, \quad Y^1 = P_1S + Y_1, \quad l^1 = L_1, \quad \lambda^{*1} = \lambda_1, \quad h^1 = L_1\log(S) + \frac{X_1L_0}{S} + H_1, \\ P^1 = 2S(L_1\log(S) - L_1 + H_1) + X_1L_0\log(S)(\frac{3}{2} + \frac{\log(S)}{2} + \frac{H_0}{L_0}). \end{aligned} \tag{S61}$$

Combining the leading order and first order terms and substituting into Eq. S57, our system of variables can be written as

$$X = S + \epsilon X_1, \quad Y = Y_0 + \epsilon(P_1 S + Y_1), \quad l = L_0 + \epsilon L_1, \quad \lambda^* = \lambda_0 + \epsilon\lambda_1,$$
$$P = S\left(H_0 + L_0\log(S) - \frac{L_0}{2}\right) + \epsilon\Big(2S(L_1\log(S) - L_1 + H_1) + X_1 L_0 \log(S)(\frac{3}{2} + \frac{\log(S)}{2} + \frac{H_0}{L_0})\Big),$$
$$h = H_0 + L_0\log(S) + \epsilon\Big(L_1\log(S) + \frac{X_1 L_0}{S} + H_1\Big). \tag{S62}$$

We are interested in the asymptotic expansion of mean curvature near the pole, which is given by

$$h = H_0 + L_0\log(S) + \epsilon\Big(L_1\log(S) + \frac{X_1 L_0}{S} + H_1\Big). \tag{S63}$$

This can be rewritten as

$$h = H_0 + L_0\log(A + S - A) + \epsilon H_1,$$
$$h = H_0 + L_0\log(A) + L_0\log(1 + \frac{S-A}{A}) + \epsilon\Big(L_1\log(S) + \frac{X_1 L_0}{S} + H_1\Big), \tag{S64}$$

where A is a constant. If $\frac{S-A}{A}$ is small, we can perform a Taylor expansion around $S = A$ to get the leading order

$$h = H_0 + L_0\log(A) + L_0\left(\frac{S-A}{A} - \frac{1}{2}(\frac{S-A}{A})^2 \dots\right)$$
$$h \sim H_0 + L_0\log(A) - L_0 + L_0\left(\frac{S}{A}\right)$$
$$h \sim H_0 + L_0\left(\log(A) - 1 + \frac{S}{A}\right)$$
$$h \sim H_0 + L_0\log(A) - L_0 + L_0\left(\frac{s}{A\epsilon}\right)$$
$$h \sim C_1 + C_2 s, \tag{S65}$$

where C_1 and C_2 are constants. This shows that the mean curvature can be approximated as a linear solution near the pole for $S \sim A$ or $s \sim A\epsilon$. In our image analysis, inaccuracies near the pole begin at orders of magnitude of 10^{-2}. At this range, we can approximate a linear solution for mean curvature.

Similarly, we consider an asymptotic expansion for ψ near the pole at leading order

$$P = S\left(H_0 + L_0\log(S) - \frac{L_0}{2}\right), \tag{S66}$$

which can be rewritten as

$$\psi = s\left(H_0 + L_0\log(s) - L_0\epsilon - \frac{L_0}{2}\right) \to \psi = s\left(D_1 + D_2\log(s)\right), \tag{S67}$$

where D_1 and D_2 are constants. We can now substitute the approximation for mean curvature and ψ near the pole into Eq. S39a and S39b to get

$$\tilde{f}_r \sim -\kappa(C_1 + C_2 s - C)(C_1 + C_2 s - C - D_2 - D_1 - D_2\log(s)) - \lambda, \tag{S68a}$$
$$\tilde{f}_z \sim -\kappa(C_2 - C'). \tag{S68b}$$

Using $\log(s) = \log(s + A - A) = \log(A) + \log(1 + \frac{s-A}{A})$ and expanding around $s \sim A$, Eq. S68b can be simplified to

$$\tilde{f}_r \sim -\kappa(F_1 s^2 + F_2 s + F_3) - \lambda, \tag{S69a}$$
$$\tilde{f}_z \sim -\kappa(C_2), \tag{S69b}$$

where F_1, F_2 are constants. We can thus approximate radial traction as quadratic in arc length near the pole, while axial traction can be correspondingly approximated as constant. In this work, we choose to start the asymptotic solution at the local minimum of mean curvature near the pole, which is $\epsilon \sim 0.1$.

2 Image analysis

Extracting forces from the membrane conformation involves multiple steps (Fig. 2):

1. First, we import images from the simulation, electron micrographs or fluorescence microscopy into the open source software 'ImageJ' and convert them into greyscale. Next, we trace the membrane contour using the Trainable Weka Segmentation plugin available in ImageJ and import the coordinates (e.g 'r' and 'z' in axisymmetric coordinates) into MATLAB.

2. The imported images are generally noisy, posing a challenge for calculating higher order derivatives along the membrane. Previous works [16] used cubic interpolating splines to fit experimental data. This has the drawback of being a linear fit in the second order, which potentially has a significant effect on the calculation of normal traction (Eq. 7a). To tackle this issue, we apply a method of derivative using continuous wavelet transform [17]. Depending on the shape, we can use different wavelet functions — e.g. a Gaussian smoothing function. A comparison of the derivatives using different methods is shown in Fig. S1. Depending on the input shape profile, we also find that other curve fits like higher order polynomial fits, Fourier fits etc. (available in MATLAB curve fitting toolbox) can provide smooth differentiable functions that are a good approximation for calculating the stress tensor. We choose the best fit based on smoothness and accuracy.

3. Next, we discretize each shape and at each point calculate the mean curvature (H_i), Gaussian curvature (K_i) and the derivative of the mean curvature — Eqs. S49 in 1D Monge or Eqs. S24 in axisymmetry — where angle ψ_i is defined such that $\tan(\psi_i) = \frac{r_i}{z_i}$.

4. Next, we need to determine the value of unknown constants, pressure difference p, tension λ, and spontaneous curvature C. Assuming that the observed shape is in mechanical equilibrium, there are three different quantities that could be used in a minimization procedure to estimate these constants; membrane energy, normal component of the force, or normal displacement. For membrane shapes that are purely controlled by mechanical forces, all three methods should give the same result, as noted by Lee et al [16]. The same group proposed the "Proximal Equilibrium Approximation" method to suppress the error due to derivative noise and to calculate the Lagrange multipliers. However, we reduce the noise error earlier by using the continuous wavelet transform. Consequently, we can rely on the more straightforward technique of "Equilibrium Force Density Minimization". The normal component of the force density ($\mathbf{f}_i.\mathbf{n}_i$), on the right hand side of Eq. 2) is zero at every discrete point on the membrane. As the membrane shape is being traced, we are able to compute the local force density as a function of unknown constants (the left hand side of Eq. 2). A global minimization on the sum of the squares of the local force density, done by 'lsqnonlin' MATLAB toolbox, provides a good approximation of the constants.

   To validate the algorithm, we have tried to recalculate the reported values for pressure, surface tension and spontaneous curvature in [16]. To get the best fit, we followed the exact same procedure as Lee et al., smoothing the shape by a cubic spline and discarding the points close to the beads. The approximated values by our method are as follows; pressure (p = $6.3\,\mathrm{mPa}$), tension (λ = $10.6\,\mathrm{k_b T}/\mu\mathrm{m}^2$) and spontaneous curvature (C = $-0.1\,\mu\mathrm{m}^{-1}$). It should be mentioned that the calculated spontaneous curvature in our optimization algorithm is a shift in mean curvature Eq. S17, while in [16], the reported spontaneous curvature is a rescaling of the principle curvature summation. Hence, if we want to compare our C with their reported value, we have to multiply it by two. Our estimated values for the three unknowns based on equilibrium force minimization are in good agreement with the values that they calculated by proximal equilibrium approximation. The difference could be the result of shape smoothness or the cut off points at the poles. After validating our method, we applied it to other experimental shapes, vesicles in [18] and podosome protrusions in [19] to calculate the spontaneous curvature field and membrane tension respectively. In the case of closed vesicles, we usually ignored the points with small radius $r = \epsilon$ because the mean curvature of those points add large error to the problem [16].

5. Finally, having mean and Gaussian curvatures along with shape constraint parameters allows us to use Eqs. 7a, 7b for axisymmetric shapes or Eqs. 9a, 9b in 1D Monge approximation to compute the surface stress tensor for a given equilibrium shape. The singularity problem at points with small radius ($r = \epsilon$) — e.g at the poles of a closed vesicle — can be solved by an asymptotic approximation for mean curvature (as described in Section 1.7).

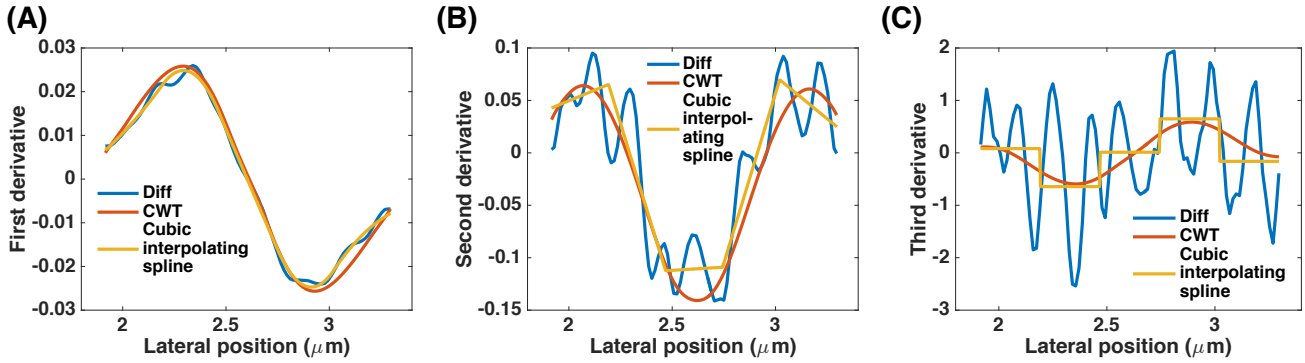

Figure S1: Three derivatives of the protrusion height profile shown in Fig. 7D using diff, cubic interpolating spline, and Gaussian smoothing wavelet transform in MATLAB. (A) First derivative of height along the lateral position of podosome protrusion. There is noise observed in the derivative calculated using diff while the derivatives due to cubic spline and continuous wavelet transform (CWT) are smooth. (B) Second derivative of height along the lateral position of podosome protrusion. There are discontinuities in the cubic spline (which is now linear) and the noise due to diff is exaggerated. CWT is smooth. (C) Third derivative of protrusion height along the lateral position of podosome protrusion. There is large amount of noise obtained using diff, while cubic spline has multiple discontinuities since it is now constant. The Gaussian wavelet function remains smooth and traces a good fit.

3 Table of notation

Table 1: Notation used in the model

Notation	Description	Units
E	Strain energy	pN · nm
γ	Lagrange multiplier for incompressibility constraint	pN/nm
p	Pressure difference across the membrane	$\mathrm{pN/nm^2}$
C	Spontaneous curvature	$\mathrm{nm^{-1}}$
θ^α	Parameters describing the surface	
W	Local energy per unit area	pN/nm
$\mathbf{r}$	Position vector	
$\mathbf{n}$	Normal to the membrane surface	unit vector
$\boldsymbol{\nu}$	Tangent to the membrane surface in direction of increasing arc length	unit vector
$\boldsymbol{\tau}$	Rightward normal in direction of revolution	unit vector
$\mathbf{a}_\alpha$	Basis vectors describing the tangent plane	
λ	Membrane tension, $-(W+\gamma)$	pN/nm
H	Mean curvature of the membrane	$\mathrm{nm^{-1}}$
K	Gaussian curvature of the membrane	$\mathrm{nm^{-2}}$
κ	Bending modulus (rigidity)	pN · nm
κ_G	Gaussian modulus	pN · nm
s	Arc length	nm
θ	Azimuthal angle	
ψ	Angle between $\mathbf{e}_r$ and $\mathbf{a}_s$	
r	Radial distance	nm
z	Elevation from base plane	nm
$\mathbf{e}_r(\theta)$	Radial basis vector	unit vector
$\mathbf{e}_\theta$	Azimuthal basis vector	unit vector
$\mathbf{k}$	Altitudinal basis vector	unit vector
$\mathbf{F}$	External force	pN
$\mathbf{f}$	Applied force per unit area	$\mathrm{pN/nm^2}$
κ_τ	Transverse curvature	$\mathrm{nm^{-1}}$
κ_ν	Tangential curvature	$\mathrm{nm^{-1}}$
τ	Surface twist	$\mathrm{nm^{-1}}$
$\tilde{\mathbf{f}}$	Traction (force per unit length)	pN/nm
$\tilde{f}_r$	Component of traction in radial direction	pN/nm
$\tilde{f}_z$	Component of traction in axial direction	pN/nm
$\tilde{f}_n$	Component of traction in normal direction	pN/nm
$\tilde{f}_\nu$	Component of traction in transverse direction	pN/nm
$\tilde{F}_z$	Calculated force in axial direction	pN
ξ	Energy per unit length	pN
M	Bending couple	pN · nm
t	Arc length around curve of revolution	nm
a	Membrane area	$\mathrm{nm^2}$
V	Confined volume by membrane area	$\mathrm{nm^3}$
s_{max}	Maximum arc length at the base	nm
R_0	Patch radius	nm
κ_0	Bending rigidity of bare membrane	pN · nm

Table 2: Notation used in the model

Notation	Description	Units
λ_0	Surface tension at boundary	pN/nm
L	Shape equation variable	nm^{-1}
x	Dimensionless radial distance	
y	Dimensionless height	
h	Dimensionless mean curvature	
c	Dimensionless spontaneous curvature	
l	Dimensionless L	
λ^*	Dimensionless surface tension	
p^*	Dimensionless pressure	
f^*	Dimensionless force per unit area	
κ^*	Dimensionless bending modulus	
κ_G^*	Dimensionless Gaussian modulus	
K^*	Dimensionless Gaussian curvature	
ζ	Dimensionless area	
A	Area of spontaneous curvature field	nm^2
ζ_{force}	Area of the applied force	nm^2
ϵ	Small parameter	
X	Rescaled parameter for x	
Y	Rescaled parameter for y	
P	Rescaled parameter for ψ	

4 Additional tether and bud formation simulations

4.1 Tubes pulled against surface tension

Motivated by Derenyi et al [20], we recreate membrane tube pulling by applying a point axial load to a circular patch of membrane. We set up the simulation to calculate the axial force needed to achieve a membrane tube of specified height and then mapped the normal and tangential traction along the membrane. We used a bending modulus of $320\mathrm{pN}\cdot\mathrm{nm}$, surface tension of $0.02\mathrm{pN/nm}$, and applied force over 1.5625% of the membrane area (approximating a point force). Eq. S25 was solved using the 'bvp4c' solver in MATLAB. Fig. S2 plots the axial and radial components of the traction along the same equilibrium shapes as in Fig. 3A–C. To compare the traction force to external force, we use Eq. S34 and modify it to be a function of nondimensional membrane area ζ (Eq.S28). For a simulation with no pressure and in axisymmetric coordinates ($dt = 2\pi r(s)$), Eq. S34 simplifies to

$$2\pi r(s)\tilde{\mathbf{f}} + \int_{\partial\omega} \mathbf{f} 2\pi R_0^2 d\alpha = 0, \tag{S70}$$

where $\mathbf{f}$ is force per unit area applied externally to the membrane. We use a hyperbolic tangent function to define the applied force, which is given by

$$\mathbf{f} = \frac{\mathbf{F}}{2\pi R_0^2 \zeta_{\mathrm{force}}} \frac{\tanh(g(\zeta - \zeta_{\mathrm{force}}))}{2}, \tag{S71}$$

where ζ_{force} is the non-dimensional area of the applied force, $g = 20$ is a constant and $\mathbf{F}$ is applied force. We can substitute Eq. S71 into Eq. S70 to get

$$2\pi r(s)\tilde{\mathbf{f}} = -\int_0^{\zeta} \frac{\mathbf{F}}{\zeta F} d\zeta, \quad \zeta < \zeta_{\mathrm{force}}, \tag{S72a}$$

$$2\pi r(s)\tilde{\mathbf{f}} = -\mathbf{F}, \quad \zeta \geq \zeta_{\mathrm{force}}. \tag{S72b}$$

Eqs. (S72a, S72b) relate external force to axial membrane traction at every point along the membrane.

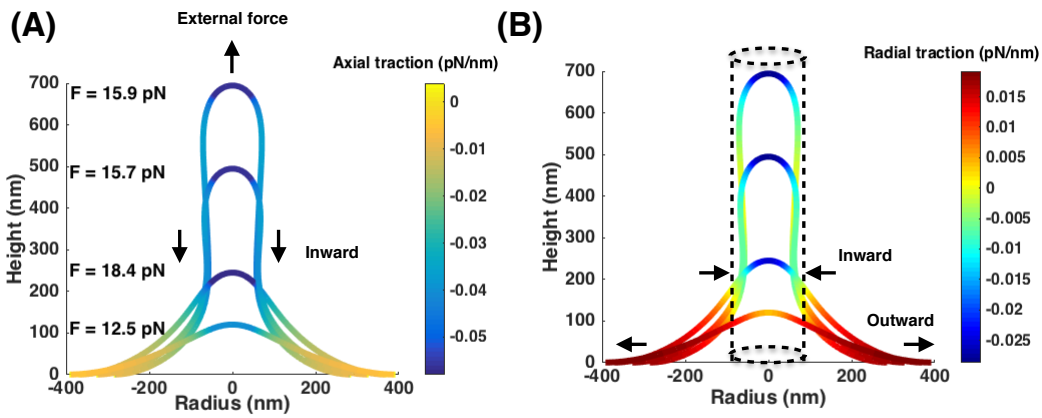

Figure S2: Axial and radial traction (Eqs. S39b, S39a) distribution plotted along the same membrane shapes as in Fig. 3A–C. (A) Axial traction distribution. The axial traction is constant along the tube. (B) Radial traction distribution. The dotted line is the stable cylindrical geometry.

4.2 Tubes pulled against pressure

In Fig. 3, we set $p = 0$ and $\lambda = 0.02\ \mathrm{pN/nm}$. However, pressure plays an important role in tether formation in certain biological contexts and thus cannot be ignored [13]. We investigated the role pressure plays during tether formation by finding pressure that produces a tube of similar radius to that obtained in Fig. 3A–C. To do this, we first define a natural length scale

for the system, R_0, by the expected equilibrium radius of a membrane tube obtained by minimization of the free energy of the membrane [20].

In absence of the pressure, external force, spontaneous curvature and Gaussian modulus, we can write the free energy Eq. S15 of the membrane as

$$E = \int_\omega (\kappa H^2 + \lambda) \mathrm{d}a. \tag{S73}$$

For a tube of length L and radius R, the free energy, ignoring the mean curvature of the cap ($H = \frac{1}{2R}$), can be written as

$$\mathcal{W}_{tube} = \left(\frac{\kappa}{4R^2} + \lambda\right) 2\pi R L. \tag{S74}$$

The balance between the surface tension, which acts to reduce the radius, and the bending rigidity sets the equilibrium radius R_0. Taking $\partial \mathcal{W}_{tube}/\partial R = 0$ we obtain

$$R_0 \equiv \frac{1}{2}\sqrt{\frac{\kappa}{\lambda}}. \tag{S75}$$

We can perform a similar analysis with pressure replacing surface tension. The free energy of the membrane Eq. S73 can be rewritten as

$$E = \int_\omega \kappa H^2 \mathrm{d}a + pV. \tag{S76}$$

Again for a tube of length L and radius R, the free energy can be written as

$$\mathcal{W}_{tube} = \left(\frac{\kappa}{4R^2}\right) 2\pi R L + p\pi R^2 L. \tag{S77}$$

Here, the balance between pressure, which acts to reduce the radius, and the bending rigidity sets the equilibrium radius R_0. Taking $\partial \mathcal{W}_{tube}/\partial R = 0$ we obtain

$$R_0 \equiv \sqrt[3]{\frac{\kappa}{4p}}. \tag{S78}$$

Comparing Eq. S78 and Eq. S75, we can find an equivalent pressure to the surface tension needed for achieving a tube of radius R_0,

$$\begin{aligned} \sqrt[3]{\frac{\kappa}{4p}} &= \frac{1}{2}\sqrt{\frac{\kappa}{\lambda}}, \\ p &= \frac{2\lambda\sqrt{\lambda}}{\sqrt{\kappa}}. \end{aligned} \tag{S79}$$

Eq. S79 gives an equivalent pressure $p = 0.3\,\mathrm{kPa}$ for a surface tension of $0.02\,\mathrm{pN/nm}$. We perform the tether pulling simulation for this value of pressure, such that the pressure acts inward for every non-zero height. Surface tension is set to zero at the base. Fig. S3A and B map the axial and radial traction along the tether and Fig. S3D and E plot the corresponding normal and tangential components. The traction distributions show similar behaviour to Fig. 3 in the main text. Using Eq. S45a, the applied force matches the difference between pressure force in the axial direction and the force due to the axial traction (Fig. S3F). Panel C plots the energy per unit length (Eq. S46a) — it shows similar behavior to Fig. 3D in the main text.

4.3 Tubes pulled against pressure and surface tension

Yeast endocytic buds experience a very large pressure on the order of $1\,\mathrm{MPa}$ [13, 21]. In Fig. S4, we perform the tether pulling simulation for pressure $1\,\mathrm{MPa}$, surface tension $0.02\,\mathrm{pN/nm}$ and bending modulus of $32000\,\mathrm{pN \cdot nm}$, suggested by [13]. Fig. S4A and B map the axial and radial tractions for four membrane shapes as the tether is pulled out. Because of the

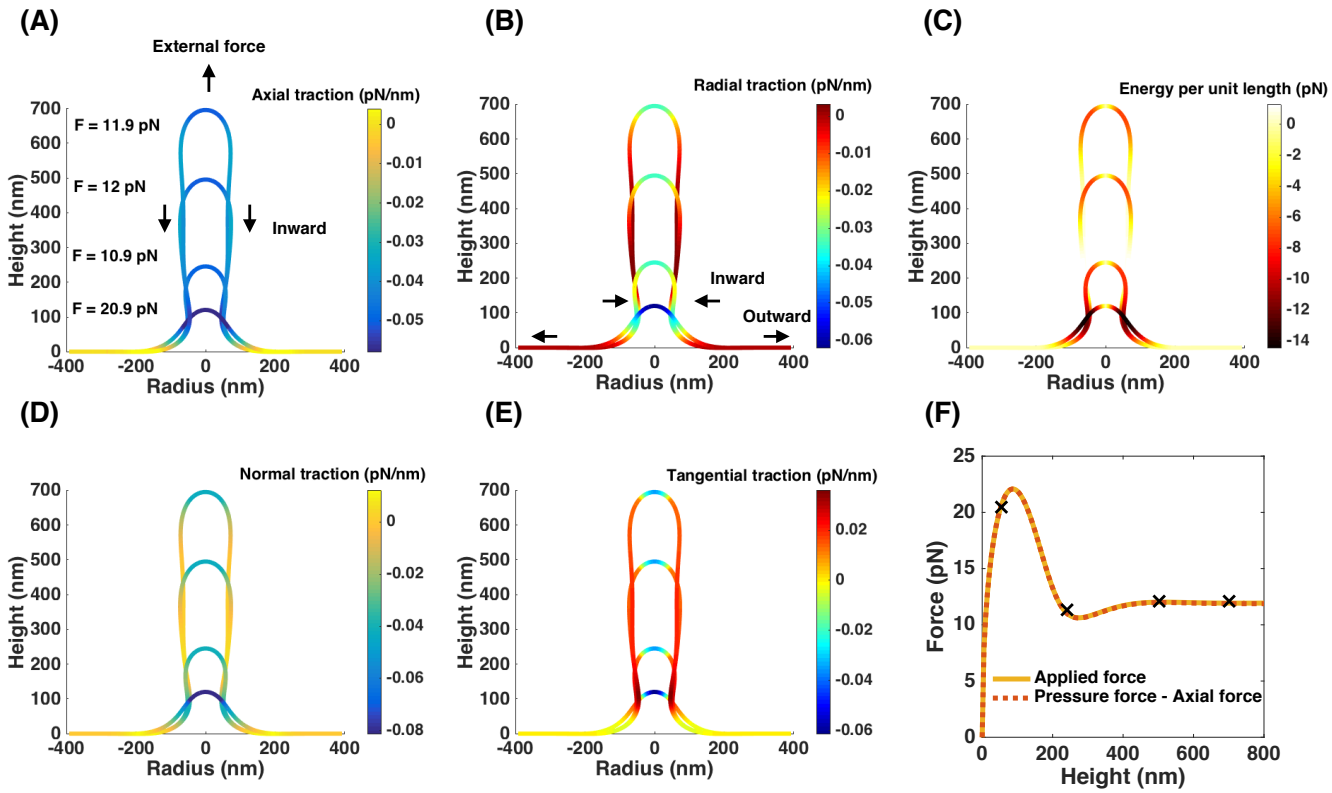

Figure S3: Tether pulling simulation for the pressure of $0.3\,\mathrm{kPa}$, bending modulus $320\,\mathrm{pN}\cdot\mathrm{nm}$, no surface tension at the boundary ($\lambda = 0$), and a point force. (A) Axial traction distribution along the tether. (B) Radial traction distribution. We find a negative value at the neck and a positive value at the base. (C) Energy per unit length (Eq. 11) plotted along the shapes. We observe a large value at the neck - predicting an 'effective' line tension of 11 pN for a tether of height 700 nm. (D) Normal traction distribution. It is large and negative over the area of applied force. (E) Tangential traction distribution. (F) Applied force and the difference between the calculated pressure and axial force (Eq. S45a) plotted as a function of tether height.

large pressure, the radius of the tether is very small. A consequence of the small radius is a positive radial traction at the neck, where the membrane wants to push out. Axial and radial traction are both constant over cylindrical parts of the tether. Energy per unit length, seen in Fig S4C shows large negative values at the neck and near the pole, similar to cases before. Fig S4D and E plot normal and tangential traction distributions along the membrane and are also qualitatively similar to the previous cases, but differ in magnitude to larger bending modulus, with tractions being almost two orders of magnitude larger. In Fig. S4F the external force is plotted vs the height of the tether and matches the difference between pressure force and axial force (Eq. S45a). In the presence of pressure, a much larger force is required to pull out the tube. The maximum force is almost 600 times larger than the case without pressure.

Using Eq. S41, we can also match the tractions at every point on the membrane to traction due to pressure and traction due to the external force. Fig. S5 shows tractions plotted along area mesh points for the tube simulation with $p = 1\,\mathrm{MPa}$ and $\kappa = 32000\,\mathrm{pN}\cdot\mathrm{nm}$ at a height of $500\,\mathrm{nm}$.

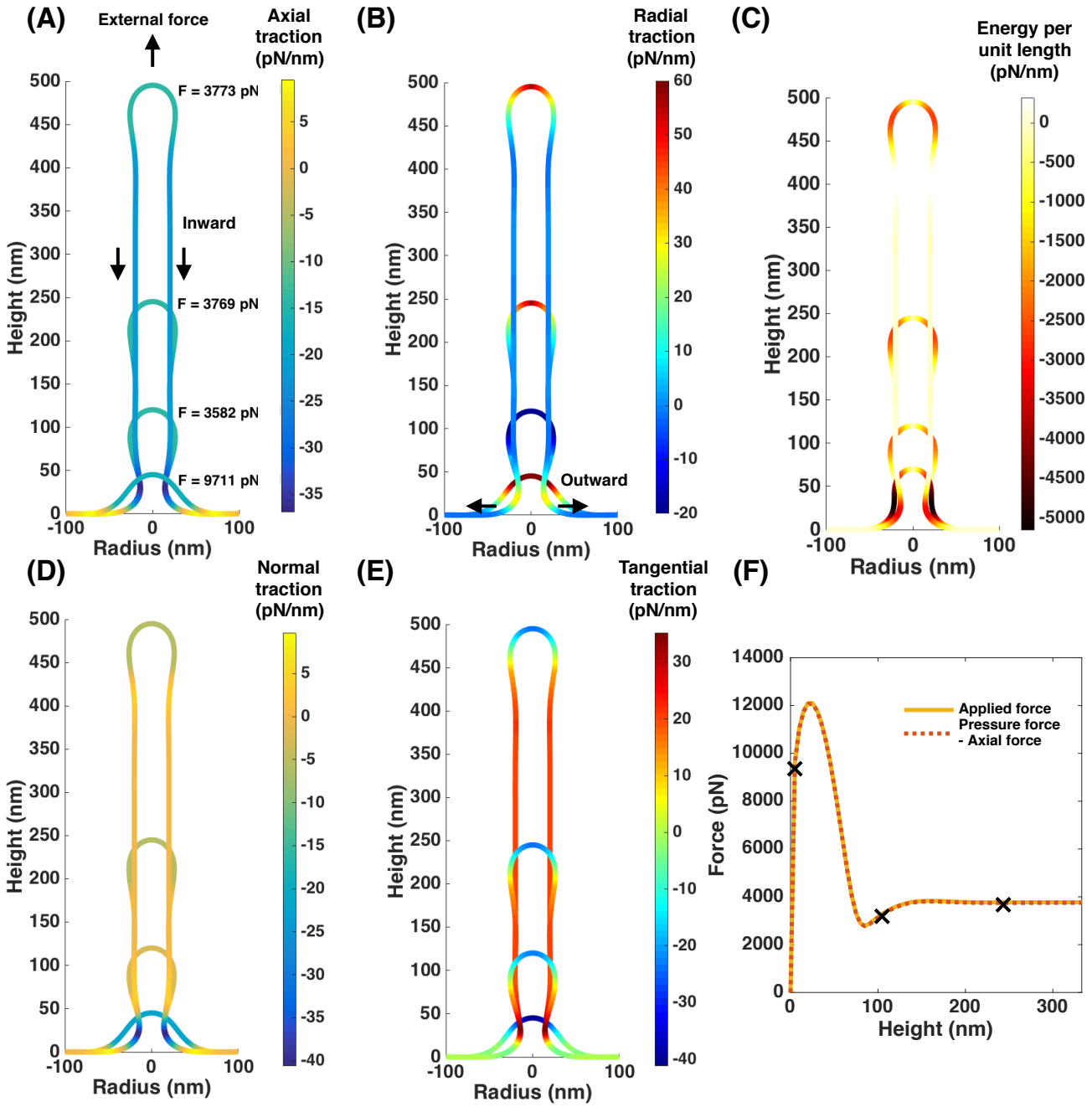

Figure S4: Tether pulling simulation for pressure $1\,\mathrm{MPa}$, surface tension $0.02\,\mathrm{pN/nm}$, bending modulus $32000\,\mathrm{pN}\cdot\mathrm{nm}$ and point force. The membrane tube is narrower and requires a much larger force to counter pressure and tension. (A) Axial traction distribution along the tether. The small positive region at the base is where pressure suddenly drops to zero. (B) Radial traction distribution. There is a large positive value at the neck, pushing against neck formation. (C) Energy per unit length Eq. 11 distribution. 'Effective' line tension at neck is 3300 pN. (D) Normal traction distribution. (E) Tangential traction distribution. There are two sign changes in tangential traction, (*i*) at the end of applied force, and (*ii*) at the neck where the tether attaches to base. A gradient in surface tension is observed at these regions. (F) Force match plotted vs height of the tether (Eq. S45a).

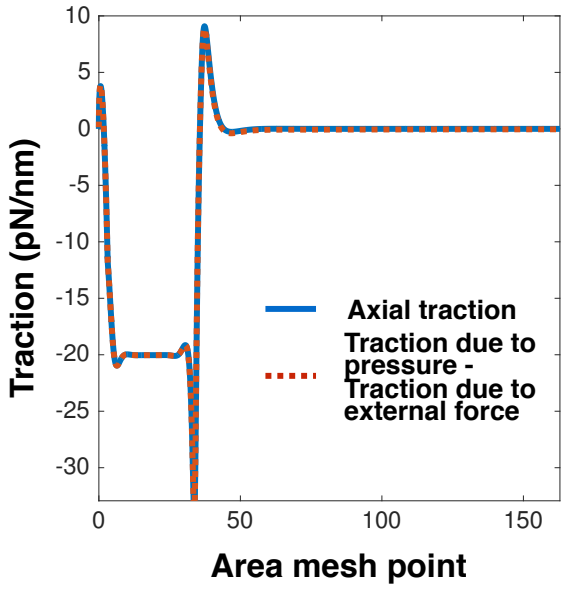

Figure S5: Tractions plotted along a tether of height $500\,\mathrm{nm}$ with the pressure of $1\,\mathrm{MPa}$, bending modulus $32000\,\mathrm{pN}\cdot\mathrm{nm}$ and surface tension $0.02\,\mathrm{pN/nm}$. Axial traction matched at every point to tractions due to pressure and external force (Eq. S41).

4.4 Axial and radial tractions in bud formation

The axial and radial tractions for the budding simulation, Fig. 4 of the main text, are shown in Fig S6.

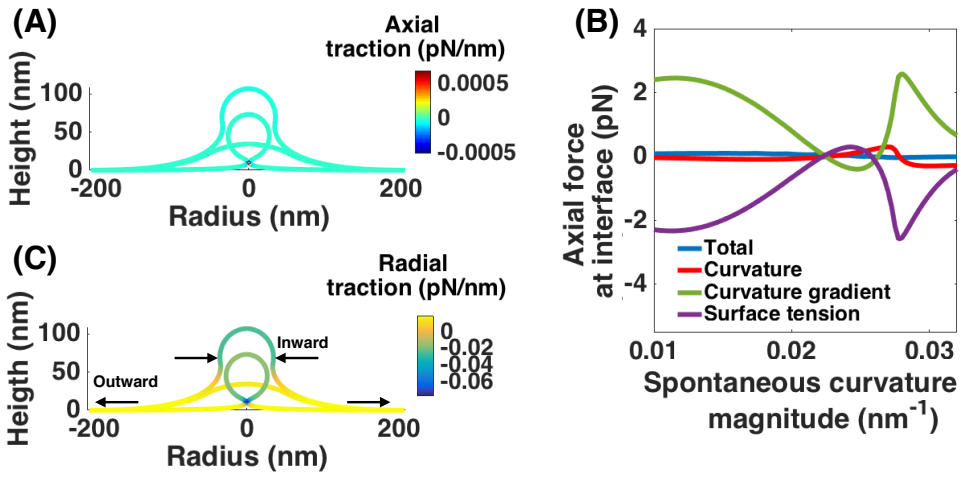

Figure S6: Bud formation from a flat membrane for increasing spontaneous curvature and a constant area of spontaneous curvature field $\mathrm{A} = 10,053\,\mathrm{nm}^2$. The spontaneous curvature magnitude increases from $C = 0$ to $C = -0.034\,\mathrm{nm}^{-1}$, the bending modulus is $\kappa = 320\,\mathrm{pN}\cdot\mathrm{nm}$ and surface tension at the edge is $\lambda = 0.02\,\mathrm{pN/nm}$. Axial traction does not play any role in invagination. (A) Axial traction along the membrane is negligible for all shapes. (B) Axial force at the interface is almost zero. Terms due to tension and curvature gradient cancel each other and force due to curvature is automatically zero. (C) Radial traction distribution for three shapes. A large negative radial traction at the neck should favor membrane scission.

The axial traction along the membrane is negligible in all the stages of bud formation (Fig. S6A). The axial force due to traction Eq. S40 depends on three different terms, curvature, curvature gradient and surface tension. The calculated axial force at the interface is zero because tension term cancels out the force due to curvature gradient and the force associated with curvature is zero by itself (Fig. S6B). This means that neck formation is purely regulated by radial stresses (Fig. S6C). For small deformations, the radial traction is positive throughout, which shows that the membrane works to oppose the deformation. However, with the formation of U shaped caps, radial traction changes sign and acts inward, representing the membrane's tendency to form small necks.

4.5 Bud formation in heterogeneous membrane with negative surface tension at boundary

In Fig. (4), surface tension at the boundary is set to $\lambda = 0.02\,\mathrm{pN/nm}$, which is close to its biological value [11, 22]. This means that at the edge where the membrane connects to the reservoir, there is a tensile stress. However, it could be possible that the boundary applies compressive stress to the domain of interest. Here, we repeat the simulation for a heterogeneous membrane with negative surface tension value at the boundary $\lambda = -0.02\,\mathrm{pN/nm}$.

Fig. S7 shows how a bud forms from an initially flat membrane by increasing spontaneous curvature magnitude from $C = 0.01$ to $C = -0.039\,\mathrm{nm}^{-1}$. Normal traction along the bud is positive, showing the membrane's resistance against deformation (Fig. S7A). Here, a larger spontaneous curvature is required to form a bud compared to Fig. 4 due to the unfavorable gradient in tangential traction at the neck – the sharp rise from negative before the neck to positive value after the neck (Fig. S7B). The energy per unit length inside the equilibrium vesicle (dashed circle) is positive indicating that the negative surface tension at the boundary is an unfavorable condition for bud formation (Fig. S7C). The initial negative energy per unit length represents membrane tendency for buckling (Fig. S7D). However, for large values of spontaneous curvature, positive energy per unit length is required to balance the negative surface pressure resulting in stable intermediate shapes (open and U shaped buds). Indeed, the positive line tension is essential to get a smooth shape evolution from a flat membrane to a closed bud.

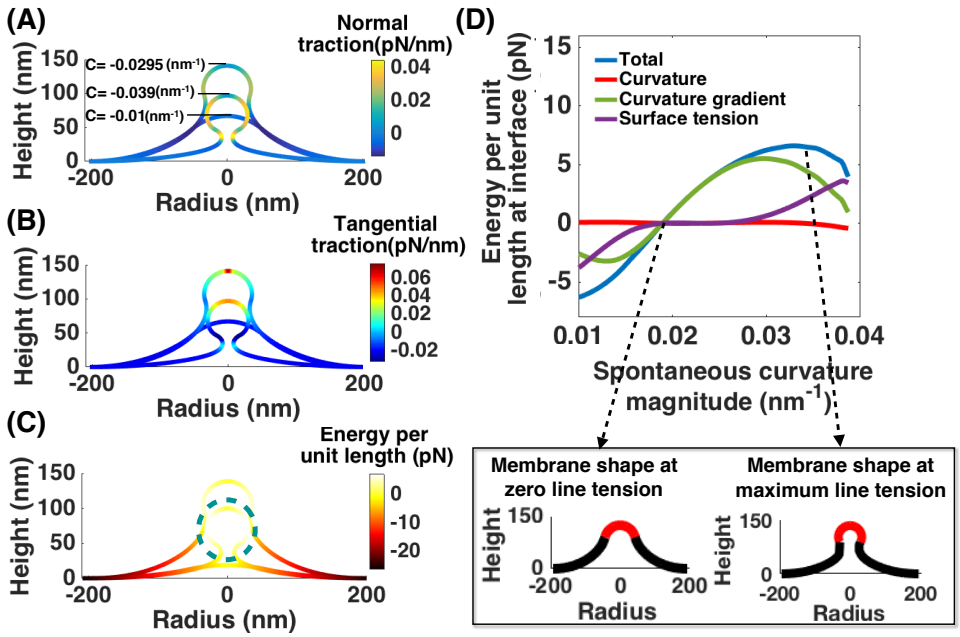

Figure S7: Bud formation with increasing spontaneous curvature magnitude ($C = 0$ to $C = -0.039\,\mathrm{nm}^{-1}$) and negative surface tension at the edge $\lambda = -0.02\,\mathrm{pN/nm}$. The area of the spontaneous curvature field and bending modulus are the same as before. Here, a larger spontaneous curvature is required to form a bud because the negative surface tension opposes the bending force. (A) Positive normal traction along the cap and bud represents the 'membrane's resistance against deformation.' (B) Tangential traction distribution along the membrane for three different shapes. In contrast to Fig. 4, tangential traction at the neck jumps from a negative value to positive one indicating the membrane's tendency to open the vesicle. (C) Positive energy per unit length inside the equilibrium vesicle -dashed circle- shows how 'effective' line tension opposes bending deformation. (D) Energy per unit length always has the same trend as curvature gradient. The subplots show the membrane configuration at zero and maximum line tension, with red lines representing the protein coat coverage for each shape.

4.6 Surface tension at the boundary regulates line tension at interface

Line tension at the interface depends on the surface tension value at the boundary (Fig. S8). For zero surface tension at the boundary, curvature gradient is the only dominant term in Eq. (S42a) and line tension is always negative (Fig. S8A). With increasing value of surface tension at the boundary, the line tension behavior can be classified in two different regimes; (1) tension dominant (2) curvature gradient dominant. In both regimes, the magnitude of line tension is larger for higher values of surface tension at the boundary. The larger line tension at the interface can be associated with an increase in bending energy, calculated by Eq. S16 (Fig. S8B).

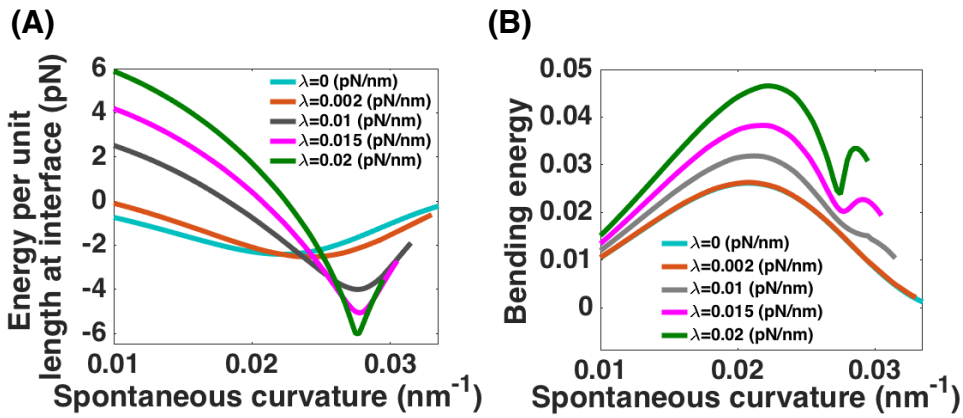

Figure S8: Increasing the energy per unit length at the interface with increasing surface tension at the boundary Eq. S42a. (A) Line tension variation at the interface vs the applied spontaneous curvature field for different values of surface tension at the edge. For large values of surface tension, the energy per unit length has a sign change from positive to negative with increasing spontaneous curvature. (B) Bending energy (Eq. S16) for different surface tension boundary conditions plotted versus the spontaneous curvature. There is an increase in bending energy cost with increase in surface tension at the boundary.

5 Podosome protrusion simulation

Fig. 7D is a finite element simulation performed using the structural mechanics module of COMSOL Multiphysics 5.2a, as described previously in [19, 23]. The formvar membrane is modeled as a cylindrical sheet with radius = 8 μm, thickness = 30 nm and is clamped at the edge. Material properties used are ρ = 6.25 $\mathrm{kg/m^3}$, E = 2.3 GPa and ν = 0.3 [23]. On the bottom surface of the cylinder, a hexagonal array of 37 two compartment modules consisting of concentric cylinders of radius = 140 nm and radius = 350 nm respectively with thickness = 20 nm is designed. The center to center distance between each module is 1.75 μm. An upward force of 10 nN is applied to the inner disc while a downward force of -(1 + α) $\times$ 10 nN is applied to the outer ring of each module, where α is a correction factor = 0.001. The model used here is the local traction-protrusion model described in [19].

6 Additional images of vesicle with phase separation

Here, we take additional images of vesicles with fluid phase co-existence from Baumgart et al. [18] and pass it through the image analysis procedure. We note that x = 0 at both poles. To obtain the asymptotic solution for the pole at the base, we rescale our variables as

$$x = X\epsilon, \quad y = Y\epsilon, \quad \psi = P\epsilon, \quad s = s_{max} + S\epsilon, \tag{S80}$$

where s_{max} is arc length at the base pole. This rescaling gives us the same asymptotic solution as Eq. S69b. Other parameters like pressure, bending modulus and surface tension of L_d and L_o phase were taken from Baumgart et al. Spontaneous curvature was estimated using equilibrium force minimization. Fig. S9 shows that the defining characteristics are similar to Fig 5 in that the normal traction is large and negative at the neck/interface of the two domains and tangential traction shows

a large gradient at the same point. Calculating the energy per unit length (Eq. S46a) for the two vesicle shapes shown in Fig. S9A and D gives values of 0.44 and 0.8 pN respectively, which is close to experimentally determined values.

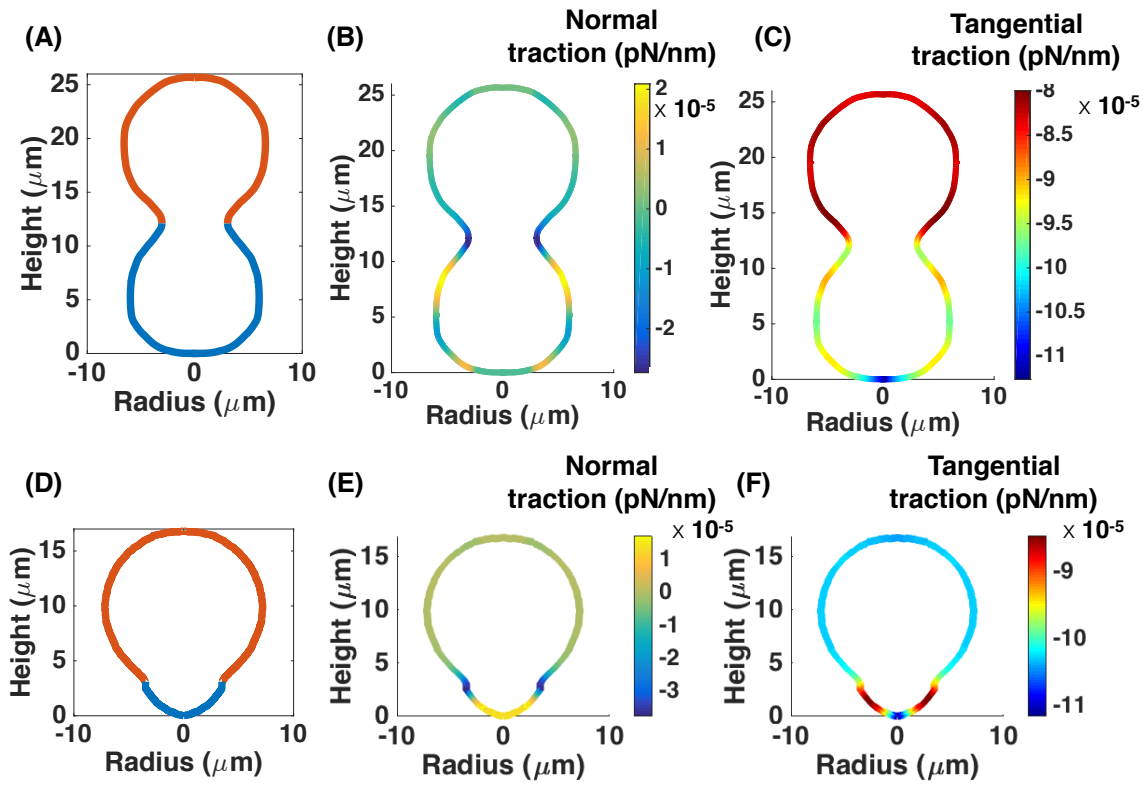

Figure S9: Normal and tangential traction distributions along vesicles with fluid phase coexistence shown in (A) and (D). Red is lipid disordered phase (L_d) and blue is lipid ordered phase (L_o). Parameters used were p = $2.8 \times 10^{-2}\,\mathrm{N/m^2}$, surface tension of disordered phase $\lambda_d = -1.03 \times 10^{-4}\,\mathrm{mN/m}$, surface tension of ordered phase $\lambda_o = -0.91 \times 10^{-4}\,\mathrm{mN/m}$, bending modulus of disordered phase $\kappa_d = 10^{-19}$ J, ratio of bending modulii $\kappa_o/\kappa_d = 5$ and absolute difference in Gaussian moduli $\Delta\kappa_G = 3.6 \times 10^{-19}$ J [18]. Spontaneous curvatures were estimated using the optimization procedure - C_d = -0.1234 $(\mu\mathrm{m})^{-1}$, C_o = -0.5763 $(\mu\mathrm{m})^{-1}$ for (A) and C_d = -1.1607 $(\mu\mathrm{m})^{-1}$, C_o = -0.1642 $(\mu\mathrm{m})^{-1}$ for (D), where C_d is spontaneous curvature of disordered phase and C_o is spontaneous curvature of ordered phase. Normal and tangential tractions were calculated using Eqs. (S44a, S43b). (B, E) Normal traction distribution along corresponding vesicle shapes. Large negative traction observed at the interface, which is also the neck. Calculating the energy per unit length (Eq. S46a) at this point predicts a line tension of 0.44 and 0.8 pN respectively — very close to the experimentally determined value of 0.67 pN. (C, F) Tangential traction distribution along the corresponding vesicle shapes. L_d phase has a larger magnitude of tangential traction than L_o phase, consistent with Fig. 5 in the main text. Gradient in a tangential traction observed at the interface.

References

1. Helfrich, W., 1973. Elastic properties of lipid bilayers: theory and possible experiments. Zeitschrift für Naturforschung C 28:693–703.

2. Miller, S. E., S. Mathiasen, N. A. Bright, F. Pierre, B. T. Kelly, N. Kladt, A. Schauss, C. J. Merrifield, D. Stamou, S. Höning, et al., 2015. CALM regulates clathrin-coated vesicle size and maturation by directly sensing and driving membrane curvature. Developmental cell 33:163–175.

3. Steigmann, D., E. Baesu, R. E. Rudd, J. Belak, and M. McElfresh, 2003. On the variational theory of cell-membrane equilibria. Interfaces and Free Boundaries 5:357–366.

4. Steigmann, D., 1999. Fluid films with curvature elasticity. Archive for Rational Mechanics and Analysis 150:127–152.

5. Rawicz, W., K. Olbrich, T. McIntosh, D. Needham, and E. Evans, 2000. Effect of chain length and unsaturation on elasticity of lipid bilayers. Biophysical journal 79:328–339.

6. Rangamani, P., A. Agrawal, K. K. Mandadapu, G. Oster, and D. J. Steigmann, 2013. Interaction between surface shape and intra-surface viscous flow on lipid membranes. Biomechanics and modeling in mechanobiology 1–13.

7. Rangamani, P., K. K. Mandadap, and G. Oster, 2014. Protein-induced membrane curvature alters local membrane tension. Biophysical journal 107:751–762.

8. Agrawal, A., and D. J. Steigmann, 2009. Boundary-value problems in the theory of lipid membranes. Continuum Mechanics and Thermodynamics 21:57–82.

9. Walani, N., J. Torres, and A. Agrawal, 2015. Endocytic proteins drive vesicle growth via instability in high membrane tension environment. Proceedings of the National Academy of Sciences 112:E1423–E1432.

10. Agrawal, A., and D. J. Steigmann, 2011. A model for surface diffusion of trans-membrane proteins on lipid bilayers. Zeitschrift für Angewandte Mathematik und Physik (ZAMP) 62:549–563.

11. Stachowiak, J. C., F. M. Brodsky, and E. A. Miller, 2013. A cost-benefit analysis of the physical mechanisms of membrane curvature. Nature cell biology 15:1019–1027.

12. Hassinger, J. E., G. Oster, D. G. Drubin, and P. Rangamani, 2017. Design principles for robust vesiculation in clathrin-mediated endocytosis. Proceedings of the National Academy of Sciences 114:E1118–E1127.

13. Dmitrieff, S., and F. Nédélec, 2015. Membrane mechanics of endocytosis in cells with turgor. PLoS computational biology 11:e1004538.

14. Deserno, M., 2004. Notes on differential geometry.

15. Fournier, J.-B., 2007. On the stress and torque tensors in fluid membranes. Soft Matter 3:883–888.

16. Lee, H. J., E. L. Peterson, R. Phillips, W. S. Klug, and P. A. Wiggins, 2008. Membrane shape as a reporter for applied forces. Proceedings of the National Academy of Sciences 105:19253–19257.

17. Jinhua, L., 2006. Application of the wavelet transforms on axial strain calculation in ultrasound elastography .

18. Baumgart, T., S. Das, W. Webb, and J. Jenkins, 2005. Membrane elasticity in giant vesicles with fluid phase coexistence. Biophysical journal 89:1067–1080.

19. Bouissou, A., A. Proag, N. Bourg, K. Pingris, C. Cabriel, S. Balor, T. Mangeat, C. Thibault, C. Vieu, G. Dupuis, et al., 2017. Podosome Force Generation Machinery: A Local Balance between Protrusion at the Core and Traction at the Ring. ACS nano 11:4028–4040.

20. Derényi, I., F. Jülicher, and J. Prost, 2002. Formation and interaction of membrane tubes. Physical review letters 88:238101.

21. Basu, R., E. L. Munteanu, and F. Chang, 2014. Role of turgor pressure in endocytosis in fission yeast. Molecular biology of the cell 25:679–687.

22. Karpova, T. S., S. L. Reck-Peterson, N. B. Elkind, M. S. Mooseker, P. J. Novick, and J. A. Cooper, 2000. Role of actin and Myo2p in polarized secretion and growth ofSaccharomyces cerevisiae. Molecular biology of the cell 11:1727–1737.

23. Proag, A., A. Bouissou, T. Mangeat, R. Voituriez, P. Delobelle, C. Thibault, C. Vieu, I. Maridonneau-Parini, and R. Poincloux, 2015. Working together: spatial synchrony in the force and actin dynamics of podosome first neighbors. ACS nano 9:3800–3813.